Expanded Research into the Relationship Between Solar Flare Magnitude and Doppler Velocities of Solar Plasma

---

Theo Stanley

Committee Members:

Dr. Thomas N. Woods – *LASP, Advisor*

Dr. Tobin L. Munsat – *Department of Physics*

Professor Mihaly Horanyi – *Department of Physics, LASP*

A thesis submitted to the Faculty of the College of Arts and Sciences of the
University of Colorado at Boulder Physics Department in partial fulfillment of the
requirements for the degree of Honors in Bachelor of Arts

Department of Physics

April 9th, 2025

This thesis entitled:

Expanded Research into the Relationship Between Solar Flare Magnitude and Doppler Velocities of Solar Plasma written by Theo Stanley
has been approved for the department of physics

Dr. Thomas N. Woods, Research Scientist and Advisor, LASP

Dr. Tobin L. Munsat, Honors Committee Member, Physics Department

Professor Mihaly Horanyi, Physics Department and LASP

Date:

The final copy of this thesis has been examined by the signatories, and we find that both the content and the form meet acceptable presentation standards of scholarly work in the above-mentioned discipline.

Dedication:

I dedicate my thesis and all related work to the late Martin Richard. I miss you every day and you continuously inspire me to strive for more.

Acknowledgements:

I would like to thank the following:

Tom Woods for being an incredible mentor and patiently answering my many questions about Solar Physics.

Rita for her invaluable assistance in deciphering the data product and being a great source of knowledge.

Bennet Schwab for his thoughtful advice and guidance throughout this process.

Don, Gabby, Phil, and the entire EVE science team for their support, listening to my presentations every Thursday, and contributing to my research journey.

Abstract:

The Doppler Velocities of nominal emission lines during solar flares directly correspond to the solar plasma's velocity. Understanding potential relationships between these emission lines and solar flares is essential for refining plasma models. The EVE instrument, with its spectral resolution of 0.1 nm, enables the measurement of Doppler shifts in solar ions, allowing for the derivation of Doppler Velocities.

In this thesis, five of the seventy nominal emission lines designated by the EVE science team are analyzed in detail. An overview of the instrument's measurements and their relevance to the central research question is also provided. Furthermore, the Doppler Velocities for the selected lines are derived. Through graphical modeling and correlation analysis, this study investigates the existence of a relationship between solar flare size and the corresponding Doppler Velocity magnitude.

Table of Contents

1: Introduction

The mechanisms driving the Sun's phenomena, particularly those that impact Earth, such as solar flares, have been the focus of scientific inquiry for centuries, with solar physics evolving significantly from early observations to modern space-based research. In 2010, the Extreme-ultraviolet Variability Experiment (EVE) was launched aboard the Solar Dynamics Observatory (SDO) to provide precise measurements of solar irradiance at X-ray and extreme ultraviolet wavelengths (0.1–106 nm). Shortly after, Hudson derived the relative Doppler Velocities of flaring plasma using EVE's data [14].

EVE filled a critical gap in solar physics, offering unprecedented insight into the behavior of solar plasma, especially during eruptive events. Key studies, such as Hugh Hudson's research on Hot Prograde Shifts, which examines the relationship between plasma flow speed and formation temperature [3], continue to refine our understanding of solar flare dynamics.

However, fundamental questions remain, particularly regarding the relationship between flare size and the magnitude of solar plasma's Doppler Velocity. Typically, X-class flares, the most powerful category of solar flares, are associated with significant energy release through the magnetic reconnection process. Given that measured Doppler shifts—and the resulting derived velocities—originate from the excitation of plasma ions during reconnection, one might expect a larger flare to produce a greater Doppler Velocity. Yet, as I will demonstrate through an analytical analysis of ions, no clear correlation exists between flare magnitude and associated Doppler Velocities.

This paper begins with an in-depth background on magnetic reconnection and the history of the EVE instrument. Following this, I introduce the ions selected for evaluation, focusing on their wavelength vs. irradiance graphs for an X-class flare observed on 2011/046. This discussion leads into the derivation of Doppler Velocities and an examination of their historical magnitude relative to flare size. Finally, I conclude with the implications of these findings and potential avenues for future research.

2: Background

2.1: Ideal Magnetohydrodynamics

Magnetohydrodynamics (MHD), first introduced by Hannes Alfvén with his conceptualization of Alfvén waves, is a mathematical model that describes the behavior of electrically conducting fluids [11]. The concept of ideal MHD is particularly important for understanding magnetic reconnection.

Alfvén's theorem, the foundation of MHD, explains how plasma behaves under ideal MHD conditions. He proposed the conservation of three key properties: magnetic flux, magnetic field lines, and, most importantly, the topology of magnetic fields. The topology of magnetic fields refers to their structural characteristics, including any twists or deformations in the field lines. While the chaotic flows of solar plasma can introduce distortions in the field, its underlying structures must be preserved due to this conservation of topology. This principle implies that changes in the structure of magnetic fields correspond to the movement of the medium, as if the magnetic field is "frozen" into the plasma [5]—a concept known as the frozen-in flux principle.

Under ideal MHD, magnetic field lines cannot "snap" and reconnect. Instead, they form a collection of twisted, chaotic structures that store vast amounts of energy.

2.1.1: Breakdown of Ideal Magnetohydrodynamics

The breakdown of ideal MHD and the subsequent occurrence of magnetic reconnection remain widely debated in the physics community. Since addressing these questions is beyond the scope of this thesis, only a brief overview is provided.

When two magnetic fields of opposite polarity come into close proximity, their interaction generates a null point—a region where the magnetic field strength approaches zero. In solar physics, a common example is an X-type neutral point. The collapse of these null points leads to the formation of current sheets, which, in turn, cause the local plasma to violate the key assumptions of ideal MHD. Specifically, the frozen-in flux principle no longer holds. The localized breakdown of ideal MHD, combined with forces from the opposing magnetic fields, triggers magnetic reconnection within the current sheet (see Figure 2.1) [4].

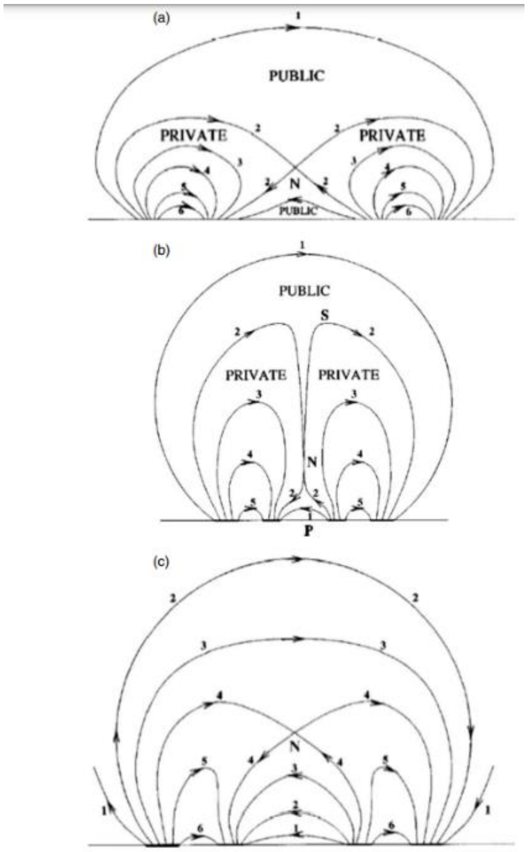

Figure 2.1: In part (a), one can see the magnetic field lines pre-reconnection. In (b), the field lines have reconnected and have returned to their ideal conditions governed by the principal laws of physics, this is commonly referred to as the relaxed state. In (c), one can see that upon returning to their relaxed state the governing equations of ideal MHD take hold due to the low resistivity of plasma on the spatial scale of the Sun. This causes them to return to a similar, twisted state as in (a). Figure borrowed from [4].

2.2 Magnetic Reconnection:

2.2.1: Challenges in Magnetic Reconnection Models

Existing magnetic reconnection models struggle to accurately account for both the rate at which reconnection occurs and the energy released into the plasma.

The widely used Sweet-Parker model predicts a reconnection rate that is significantly slower than what is observed on the Sun. Another model, developed by Petschek, incorporates slow-moving shocks to accelerate plasma. While this approach yields more physically accurate predictions, the formation of slow-moving shocks requires highly specific conditions that are not broadly applicable to most of the Sun’s reconnection events.

2.2.2: Magnetic Reconnection Process

Regardless of the exact model, the fundamental process begins at the breakdown of ideal MHD. Once the highly twisted magnetic field lines are free to return to a lower-energy state, they "snap" and reconnect within the current sheet, releasing their stored energy into the surrounding plasma. This energized plasma, along with its excited ions, is then accelerated outward along the current sheet (see Figure 2.2).

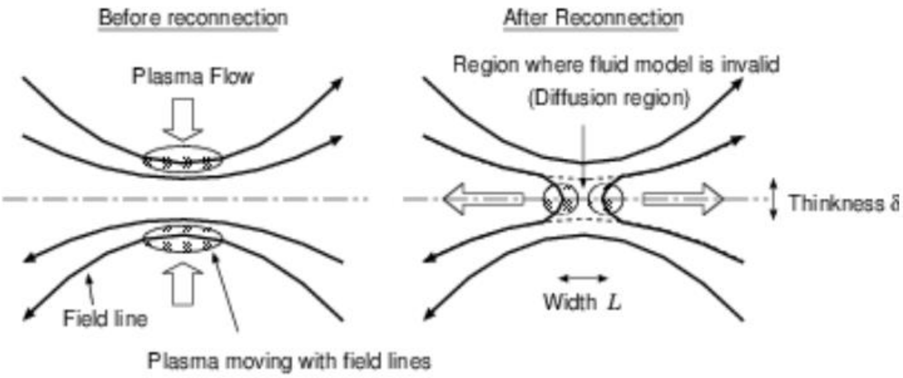

Figure 2.2: Take L to be the length chosen by Sweet-Parker; the local reconnection of the lines follows from this model. The small thickness of the current sheet obeys the theoretical numbers, while the width L can be assumed to be small in terms of solar scale. The field lines can diffuse through the current sheet during the reconnection process following the breakdown of Ideal MHD. Figure borrowed from [9].

In the magnetic reconnection model shown in Figure 2.1, field loops typically extend into the corona, allowing plasma to be ejected either upward into the corona (known as upflows) or downward toward the chromosphere (referred to as downflows) [17].

2.3: Solar Flares

Connecting magnetic reconnection to solar flares requires a review of flare development and classification. Solar flares generally occur in two main phases: impulsive and gradual.

2.3.1: Impulsive Phase

The impulsive phase of a solar flare is typically identified by the emission of hard X-rays, which can also be observed as a rise in soft X-ray emissions detected by the Geostationary Operational Environmental Satellite (GOES). This phase marks the primary energy release from the reconnection event and includes hard X-ray emissions from plasma downflows impacting the footpoints of magnetic field loops in the chromosphere. This process, known as chromospheric heating, causes the expansion of plasma from the chromosphere into the corona. As the plasma cools, it emits soft X-rays in a process commonly referred to as chromospheric evaporation.

Depending on the model, chromospheric evaporation can occur during either the impulsive or gradual phase of the flare.

Furthermore, since magnetic reconnection occurs during the impulsive phase, the associated plasma upflows and downflows have been extensively studied. Researchers have established a relationship between plasma flow speed and formation temperature:

- Plasma with formation temperatures above 4 million Kelvin (MK), known as hot coronal lines, is typically associated with upflows (blueshifted Doppler shifts).
- Plasma with temperatures below 0.3 MK, which includes chromospheric and transition region lines, is generally linked to downflows (redshifted Doppler shifts).

For plasma with temperatures between 0.3 MK and 4 MK, classified as warm coronal lines, the relationship is less well defined. However, there is some consensus on the existence of a 2 MK "breaking point," where emissions transition from exhibiting a blueshift to a redshift [17].

2.3.2: Gradual Phase

The gradual phase begins at the soft X-ray peak of the flare and continues through its decay. During this phase, the coronal loops, which expanded due to heating in the impulsive phase, relax back to their pre-flare state.

The duration of the gradual phase varies significantly, suggesting the possibility of ongoing reconnection events or continued heating from unresolved sources [17]. Emission lines measured by EVE with formation temperatures below 0.1 MK are often associated with this phase. While the relationship between temperature and flow speed is less well-defined in the gradual phase, it generally follows the same trend observed during the impulsive phase.

2.3.3: Flare Sizes

In modern Solar Physics, flare size is defined based off the peak flux ($\frac{W}{m^2}$), for Soft X-Rays between 0.1-0.8 nm. Five categories of Flare exist: A, B, C, M, X. Additionally, to clarify terminology, flare size can also be used to define the physical size of a flare, but in the context of this paper it references its magnitude in terms of peak flux.

A, and B class flares will not see discussion in this paper, and due to their small size, are not measured by the EVE science team.

Flare Class:	**Peak Flux Range ($\frac{W}{m^2}$)**
C	$1 * 10^{-6} \leq C < 1 * 10^{-5}$
M	$1 * 10^{-5} \leq M < 1 * 10^{-4}$
X	$1 * 10^{-4} \leq X$

Figure 2.3: A table displaying the relationship between each flare class and their respective flux range.

Flare classification follows a logarithmic scale, meaning each class is 10 times stronger than the previous one. Additionally, within each class, flares are further ranked on a linear scale from 1 to 9.9. For example, an M2.2 flare is 10 times weaker than an X2.2 flare.

2.4: The EVE Instrument

Shifting focus from magnetic reconnection and flare development, it is important to discuss the instrument used to observe these events: EVE (Extreme-ultraviolet Variability Experiment).

EVE utilizes two Multiple EUV Grating Spectrographs (MEGS-A and MEGS-B) to measure wavelength and irradiance. MEGS-A captures spectral measurements in the 5–37 nm range, while MEGS-B covers the 35–105 nm range. At launch, EVE provided full coverage of 5–105 nm with a 0.1 nm spectral resolution and an integration time of 10 seconds, offering an unprecedented level of insight into the solar spectrum [15].

However, in 2014, a capacitor short in MEGS-A CCD power supply caused the loss of MEGS-A (5–35 nm range). Additionally, MEGS-B had unexpected degradation after launch in the 70-106 nm range. To adapt, the observation cycle was modified so that MEGS-B now operates on a 3-hour daily cycle. If a solar flare is detected by the modified EVE flight software, MEGS-B solar observations automatically start to ensure the event is fully captured [16].

The primary goal of EVE was to characterize solar irradiance over time and explain fluctuations in its variability. However, due to the instrument's stability and sensitivity, Hudson realized it could also be used to derive Doppler shifts from its data.

Despite this capability, EVE has two main limitations. The first is its limited spectral resolution of 0.1 nm, which poses challenges for precise measurements. The second it's a simple spectrograph design without a front-end telescope, meaning MEGS-A and B provide only "Sun-as-a-star" measurements, which lack spatial resolution [14].

Fortunately, other instruments aboard the SDO, such as the Atmospheric Imaging Assembly (AIA), provide spatial data on flare locations. Through relatively straightforward derivations, researchers can correlate EVE's irradiance measurements with locational data from AIA [16]. However, the coarse spectral resolution of 0.1 nm remains a persistent challenge for researchers.

2.4.1: Line Blends

The Sun contains a wide range of ions at varying temperatures and wavelengths, leading to an immense number of nominal emission lines during solar flares. In many cases, multiple emission lines have Doppler wavelengths that differ by less than 0.1 nm, making it impossible to distinguish between individual ions. This phenomenon, known as line blending, complicates spectral analysis. While line blending presents an interesting avenue for future research, it poses significant challenges when studying broader solar relationships. In my investigation of the magnitude of Doppler Velocity versus solar flare size, blending introduces a persistent source of uncertainty, making it difficult to extract clear and conclusive trends.

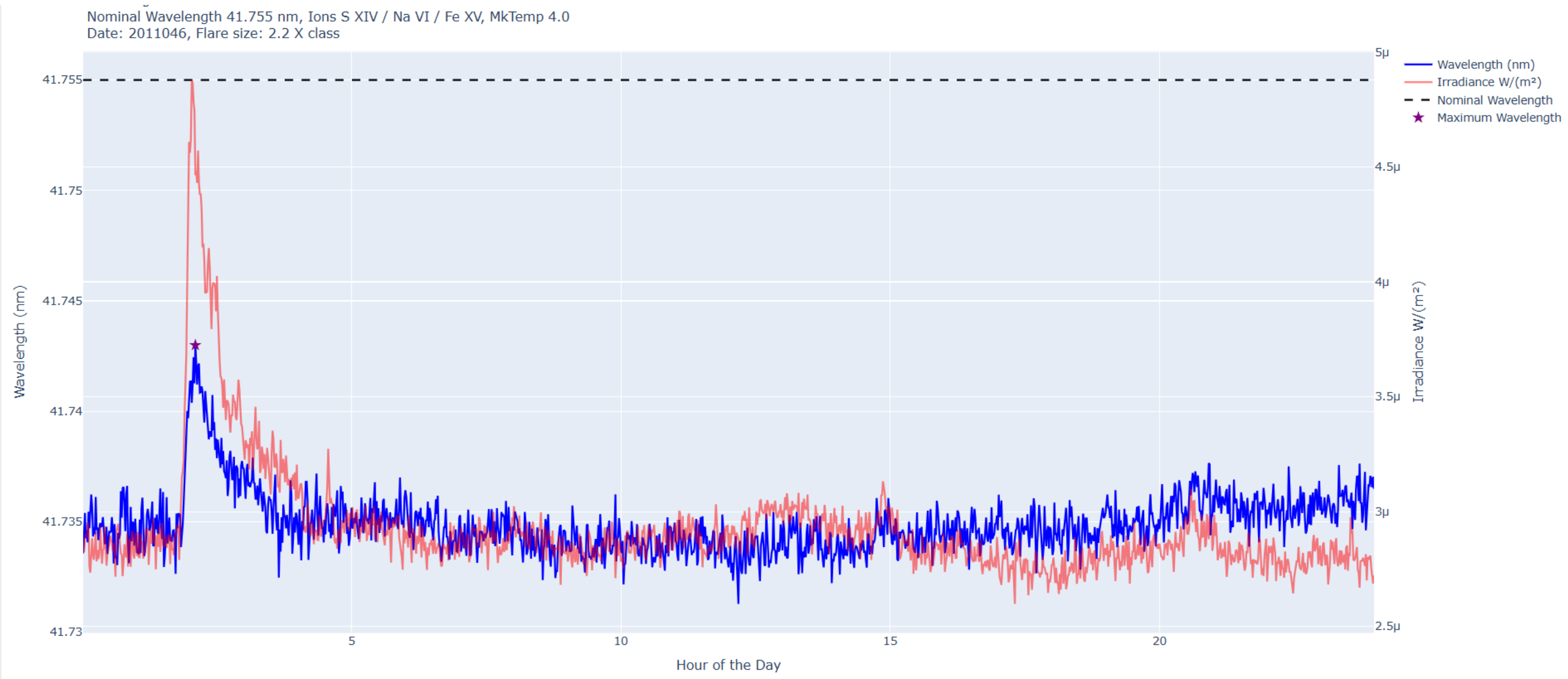

Figure 2.4: A graph of wavelength 41.755 nm (S XVI) for the date 2011/046. The varying irradiance (Red) has the Wavelength (blue) overlayed, with the nominal wavelength (black dashed) providing a reference point. The different phases of the flare can be observed. The increasing irradiance corresponds to impulsive phase, while the peak and later decreasing irradiance correlate to the gradual phase. An increase in wavelength away from the background wavelength indicates a clear redshift.

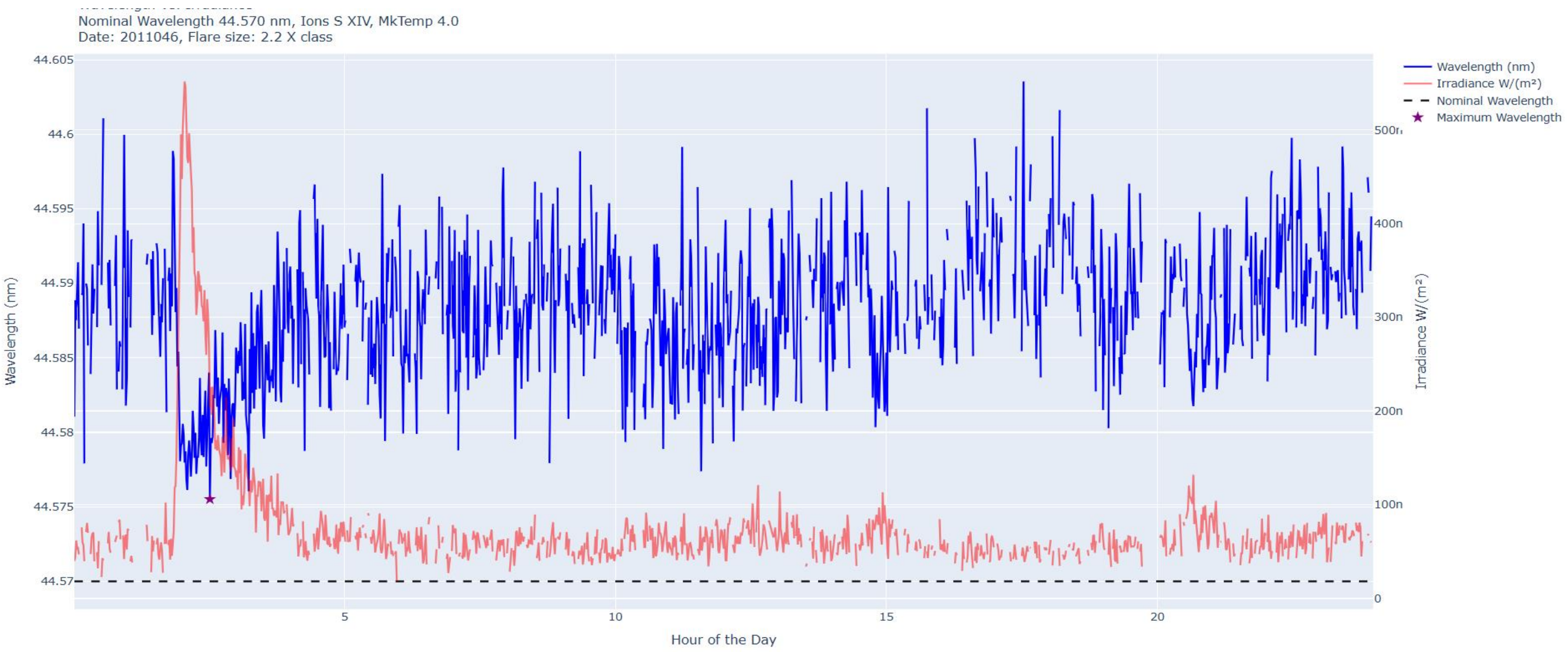

Figure 2.5: Another graph of the S XVI Ion, except at wavelength 44.570 nm. In this figure, there is a clear blueshift, or decrease in wavelength.

One of the primary issues with line blending is the introduction of false spectral trends. In Figures 2.4 and 2.5, two different nominal wavelengths from the EVE Level 4 data product can be observed, both featuring S XVI as the dominant ion contributing to the irradiance peak. However, the 41.755 nm line includes a variety of additional ions and exhibits completely different behavior compared to the 44.570 nm wavelength, where the latter shows a blueshift while the former demonstrates a redshift. Hence, the 41.755 nm is identified as a line containing significant blends.

In Section 3.1, I detail the method used to identify line blends and select nominal wavelengths for analysis. My initial focus was on minimizing line blending in the dataset, and I took great care to exclude any blended lines from my final analysis to ensure the accuracy of my results.

2.5: The Level 4 Data Product

The EVE science team provides a data product aimed at ensuring ease of access for fellow researchers, known as the Level 4 Data Product. I worked extensively on improving the quality and usability of this product.

The organization of the Level 4 Data Product is critical to understanding my methodology. On a general level, the data for each day is processed using IDL functions and then sorted into Flexible Image Transport System (FITS) files for easier access. Each FITS file contains five variables: 'LinesMeta', 'LineFitParams', 'FlareFitParams', 'LinesFitAccuracy', and 'LinesData'. These bins contain arrays representing data, errors, and other important values for the EVE mission. Most of the information in the FITS file is related to the seventy nominal emission lines chosen by the EVE science team. However, I incorporated only four of these bins into my analysis: 'LinesMeta', 'LineFitParams', 'FlareFitParams', and 'LinesData'.

2.5.1: LinesMeta

The 'LinesMeta' variable contains general information about each of the seventy nominal emission lines, including the nominal wavelength, ions associated with each line, and the average temperature (in million Kelvin) of each line.

2.5.2: LineFitParams

The 'LineFitParams' variable provides the measured wavelength data as well as the parameters used to evaluate the validity of the Gaussian fit, including error values for each wavelength. To organize the data, I restructured the arrays so that their format appeared as [1440, 70], where each row represents a minute of the day, and each column corresponds to one of the nominal wavelengths.

2.5.3: FlareFitParams

Similarly, the ‘FlareFitParams’ variable contains data similar to ‘LineFitParams’, but with additional arrays. The key difference between ‘FlareFitParams’ and ‘LineFitParams’ is the inclusion of the Pre-Flare Time and Flare Wavelength arrays. The Pre-Flare Time refers to the Julian Day when no flare had occurred, providing a baseline for the background wavelength of the line before the flare (discussed further in Section 3.2).

Furthermore, the difference between the wavelength and flare wavelength arrays remains important to this paper’s clarity. Until December 2024, EVE only provided the full wavelength spectrum for flare campaigns. These measurements give a good idea of the given day’s line trends, however, make careful analysis of tendencies during the actual flare more difficult. The flare wavelength array follows the same formatting as the wavelength array [1440,70] but stores only values at the peak of the fitted data; wavelength measurements that occur during the flare. My discussion of results in Section 3 focuses mainly on the flare wavelength values, with this array getting used for my Doppler Velocity derivations.

2.5.4: LinesData

Finally, the ‘LinesData’ variable provides broader context for the day represented by the FITS file. It contains metadata such as the year and day ([YYYY/DDD]) the data was recorded, as well as flags indicating the start and end times of a flare, as well as whether the flare is increasing or decreasing. Importantly, ‘LinesData’ also stores the measured line irradiances in an array of shape [1440, 70], corresponding to each nominal emission line.

3: Analysis of Data:

A significant portion of my thesis work focused on interpreting and analyzing the data provided by the Level 4 Product. To investigate any potential correlation between flare size and the magnitude of corresponding Doppler Velocities of nominal solar emission lines, I first needed to narrow down the list of potential line candidates. The EVE database contains thousands of flare events, each with measurements for each of the seventy nominal emission lines. Although the code I developed could be adapted to analyze all these lines, time constraints required that I be more selective in my research approach.

3.1: Wavelengths and Ions

There were several key factors I had to consider when choosing the nominal wavelengths and their associated ions for analysis. As previously mentioned, the 0.1 nm spectral resolution of the EVE instrument can sometimes lead to misleading data. In the first few months working with the EVE science team, I focused heavily on reducing blended elements in the Level 4 data product. In addition to ensuring that the wavelengths I used did not contain significant blends, it was also essential that each line had a corresponding comparison line. The criteria for the comparison line were straightforward: it needed to be another line without blends and at the same temperature.

To evaluate the blends of each wavelength, I employed an IDL function written by Tom Woods that analyzed each of our nominal wavelengths using the Chianti database. The returned table (Figure 3.1) contained the relative abundances of the ions present for a given wavelength at temperatures from 0.1-20 MK. The EVE science team defines unblended lines as those where a single ion of high abundance, approximately 95% or more, has a contribution to the irradiance peak at least 10 times greater than any other reported ion at different temperatures.

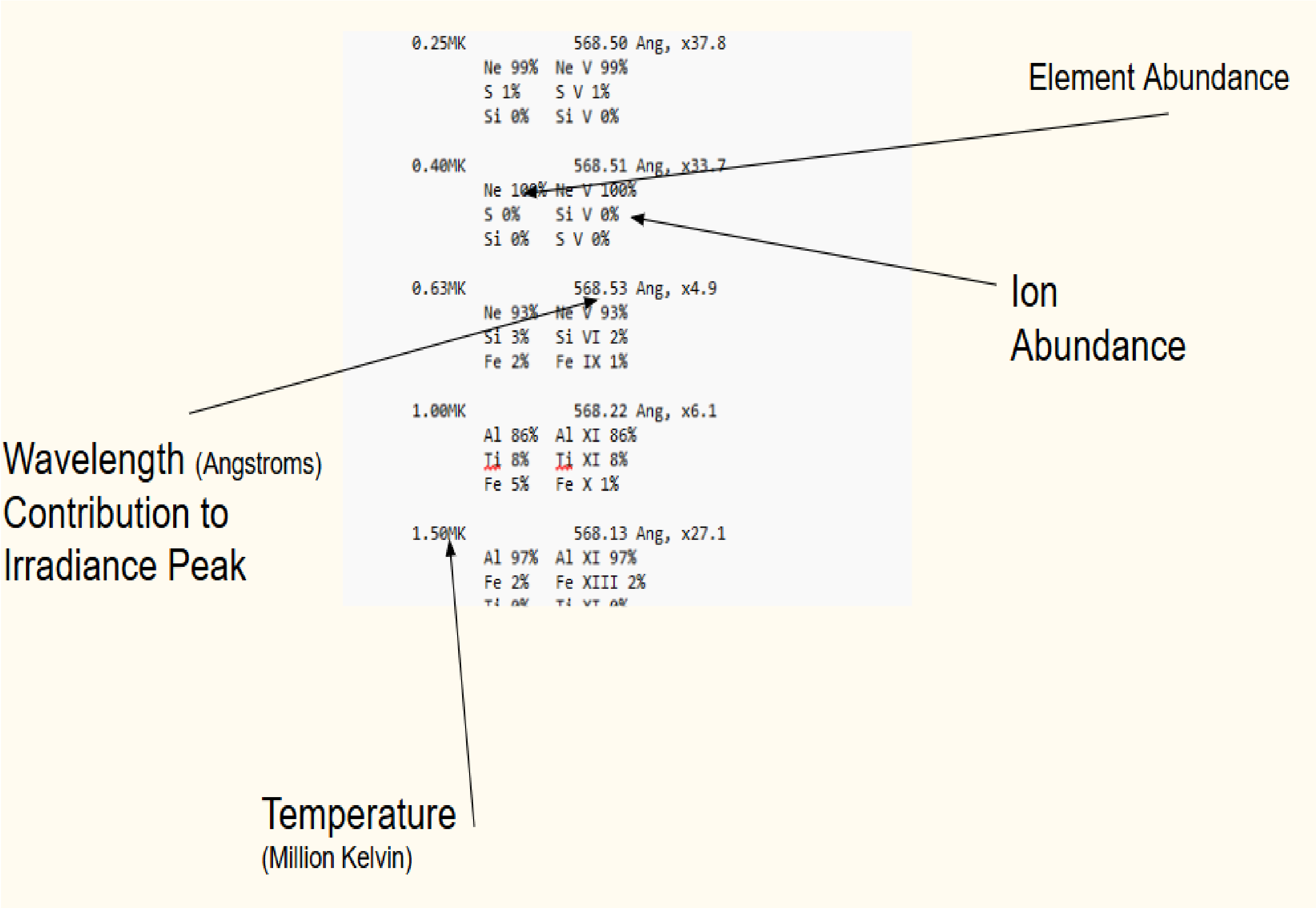

```
0.25MK          568.50 Ang, x37.8
        Ne 99%  Ne V 99%
        S 1%    S V 1%
        Si 0%   Si V 0%

0.40MK          568.51 Ang, x33.7
        Ne 100% Ne V 100%
        S 0%    Si V 0%
        Si 0%   S V 0%

0.63MK          568.53 Ang, x4.9
        Ne 93%  Ne V 93%
        Si 3%   Si VI 2%
        Fe 2%   Fe IX 1%

1.00MK          568.22 Ang, x6.1
        Al 86%  Al XI 86%
        Ti 8%   Ti XI 8%
        Fe 5%   Fe X 1%

1.50MK          568.13 Ang, x27.1
        Al 97%  Al XI 97%
        Fe 2%   Fe XIII 2%
        Ti 0%   Ti XI 0%
```

Figure 3.1: From this table, it is evident that this line is blended. Ne V at 0.25 MK has an overall contribution of x37.8, which is not 10 times greater than the next highest contributing ion, Al XI at 1.5 MK. However, the figure is truncated, so the analysis presented here is not entirely comprehensive.

Following my investigation into the line blends of the nominal wavelengths, I selected two lines at different temperatures that did not exhibit any significant blending. The need for lines at different temperatures arose from the predicted behavior of downflows and upflows. To accurately address my research question, I required lines that captured the redshift and blueshift tendencies of specific temperature groups. These selected wavelengths then served as a reference for finding my comparison lines. Ultimately, I identified five nominal wavelengths in the EVE

Level 4 product that exhibited no blending and could be used to confirm the Doppler behavior of one another.

The nominal wavelengths that will appear for the rest of this paper are as follows:

Fe XVI (36.076 nm, MK Temp 2.5)

Mg VII/ Mg IX/ Fe XIII (36.812 nm, MK Temp 1.5)

Si XII (49.941 nm, MK Temp 2.5)

Si XII (52.066, MK Temp 2.5)

Al XI (55.002 nm, MK Temp 1.5)

The Mg and Al lines both represent one temperature group, 1.5 MK, while the two Si lines and Fe line provide us with analysis of 2.5 MK. Both groups fall within the classification of warm coronal region lines, making their expected Doppler shifts difficult to predict. However, as noted in Section 2.3.1, a loose cutoff point of 2.0 MK has been established. In practice, one might expect Si and Fe to exhibit more frequent blueshifts, while Mg and Al demonstrate a semi-consistent redshift [17].

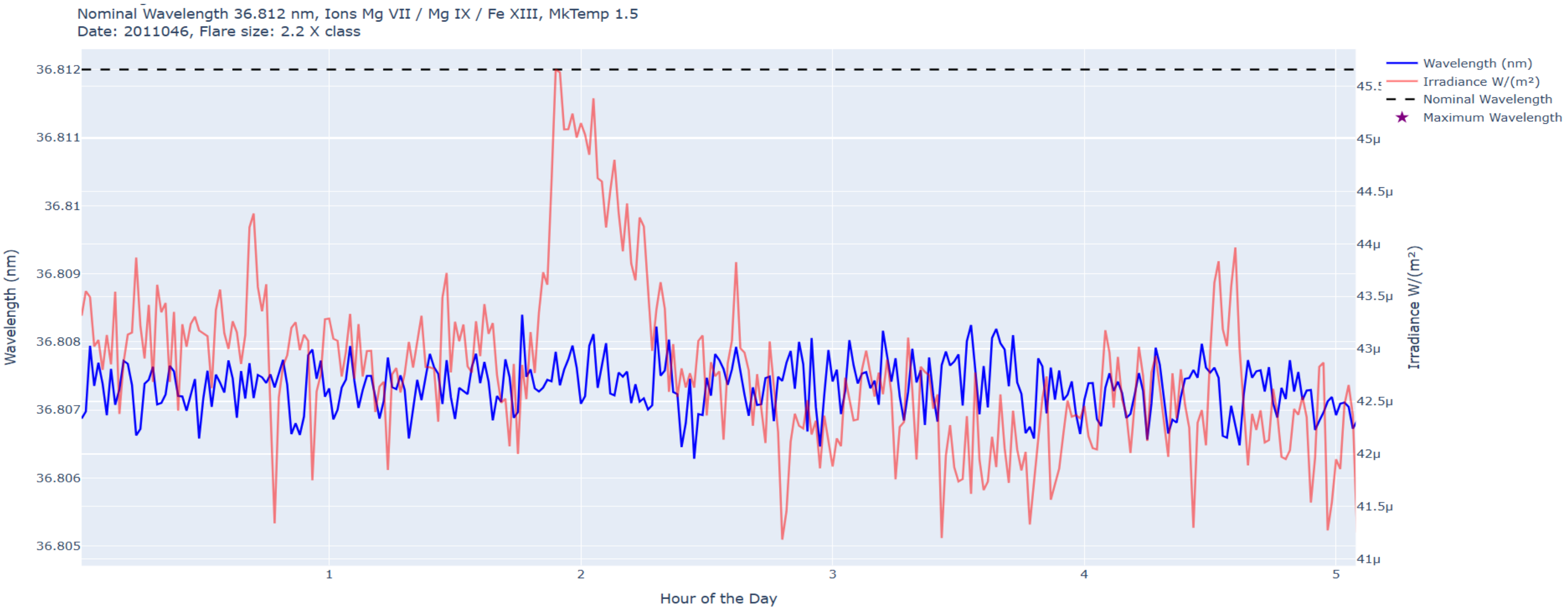

Figure 3.2: The wavelength and irradiance graph for 36.812 nm (Mg VII) on 2011/046. The graph is zoomed in to better highlight behavior during the flare. The Doppler shift of this wavelength is difficult to discern, and the nominal emission line seems to not react to flare event. Graph formatting follows that of Figure 2.4.

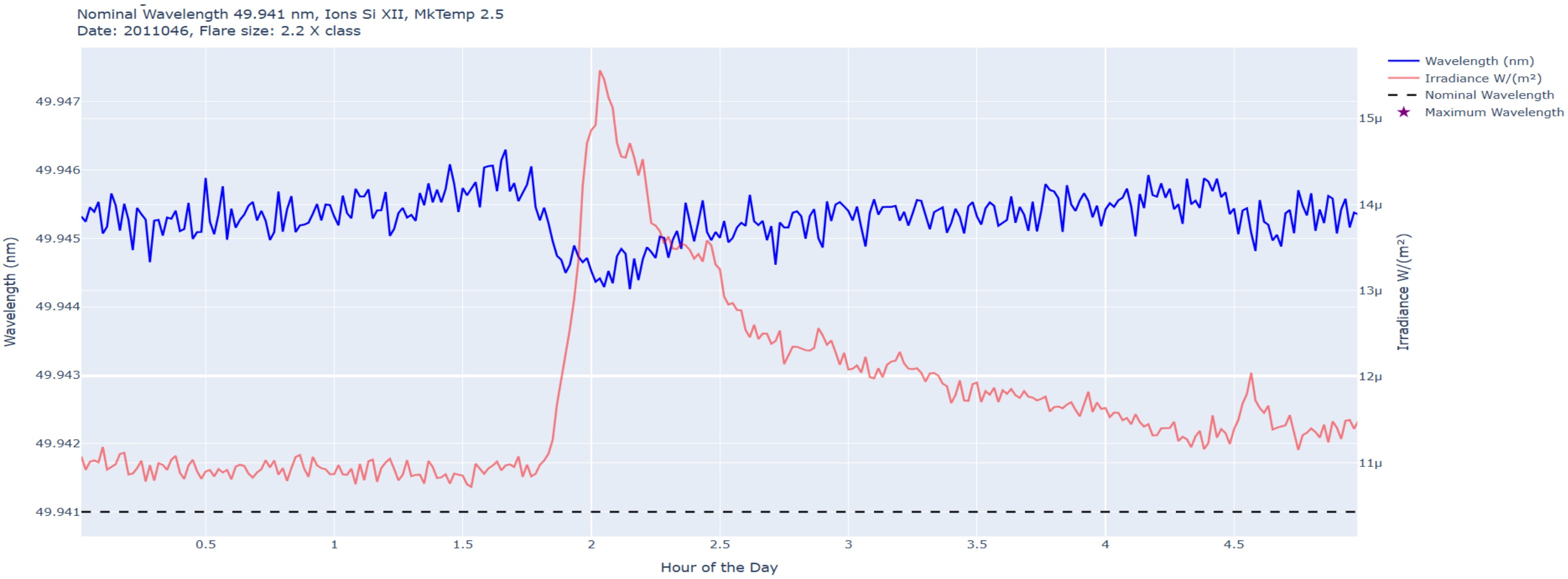

Figure 3.3: Wavelength and irradiance graph for 49.941 nm (Si XII), a blueshift is seen as the wavelength decreases during the flare.

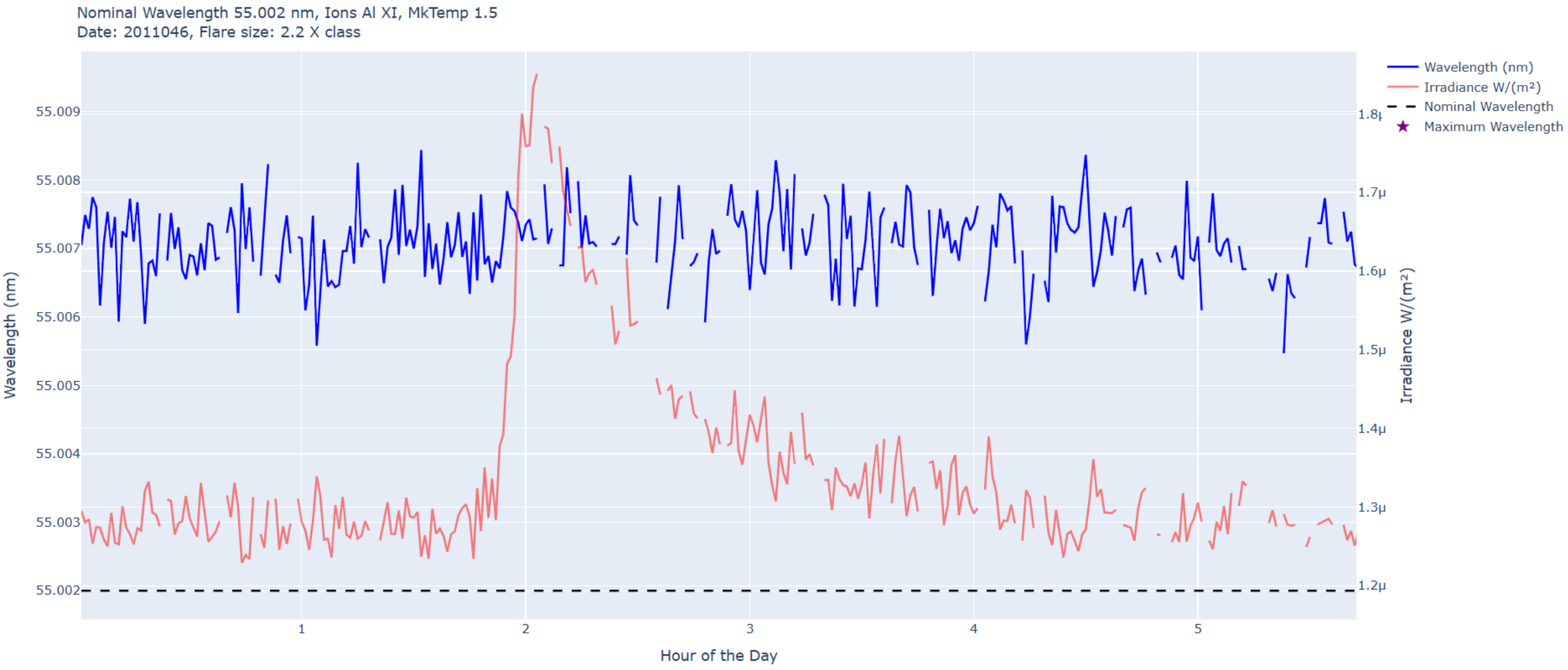

Figure 3.4: Like the other reference wavelength at 1.5 MK, 55.002 nm (Al XI) exhibits highly challenging behavior to interpret. The missing wavelength and irradiance data observed during the flare can be attributed to the EVE science team flagging these values as invalid Gaussian fits during processing

I would like to highlight some apparent Doppler behavior in Figures 3.2, 3.3, and 3.4 that is not caused by the flare event. In the absence of the flare, Figures 3.3 and 3.4 exhibit a redshift relative to the nominal wavelength (black dashed line), while Figure 3.2 shows a blueshift. This behavior arises from two main factors. First, the sinusoidal orbit of the satellite, which is not incorporated into these figures, can cause apparent shifts in a wavelength. However, this behavior is largely insignificant when compared to the shifts caused by the solar flare itself. Second, the imprecise nature of calculating nominal emission lines contributes to this shift. The value of each nominal emission line is derived from the calculated emission wavelength of an excited ion returning to its ground state. Due to the chaotic nature of solar plasma, this often represents only a rough estimate at best. As will be demonstrated in the following section, using a derived background wavelength in conjunction with the flare wavelength provides a clearer representation of the behavior of each line.

For 2011/046, the behavior of the 49.491 nm wavelength (Si XII) offers an easier analysis. A clear blueshift is observed during the period of increasing irradiance, corresponding to the impulsive phase of the flare. This blueshift starts to dissipate as the flare reaches its peak irradiance, with the measured wavelength returning to its pre-flare state as the flare's irradiance decreases. This aligns with the loose expectations I described earlier in this section.

However, no clear manifestation of a blue or redshift can be inferred from the 55.002 nm wavelength (Al XI) graph (Figure 3.4). Similarly, for the comparison line at 1.5 MK, the 36.812 nm (Mg VII) graph displays behavior that is equally difficult to interpret (Figure 3.2). While complex Doppler shifts are expected for warm coronal lines, the fragmented nature of the data for this day, combined with the lack of any clear Doppler behavior, highlights the need for a different analysis approach to study the EVE line shifts.

3.2: Flare Wavelength:

Now, let us reference the flare wavelength and irradiance graphs for my nominal emission lines. These graphs provide a more detailed view of the wavelengths measured during the flare event but come at the cost of losing information about the background trends surrounding the nominal wavelength.

To address this issue, I used the pre-flare time data in the Level 4 data product to index the wavelength array. The pre-flare time represents a period identified by the EVE processing algorithm when no flare has occurred, but measurements for the nominal wavelengths are still available. I used the pre-flare time as an index for the wavelength array, and this reference wavelength was then averaged over the surrounding ten-minute period to produce a background wavelength value. This background wavelength value serves as an estimate of the ion's behavior before the flare event and provides a useful benchmark for interpreting the Doppler shifts observed during the flare event.

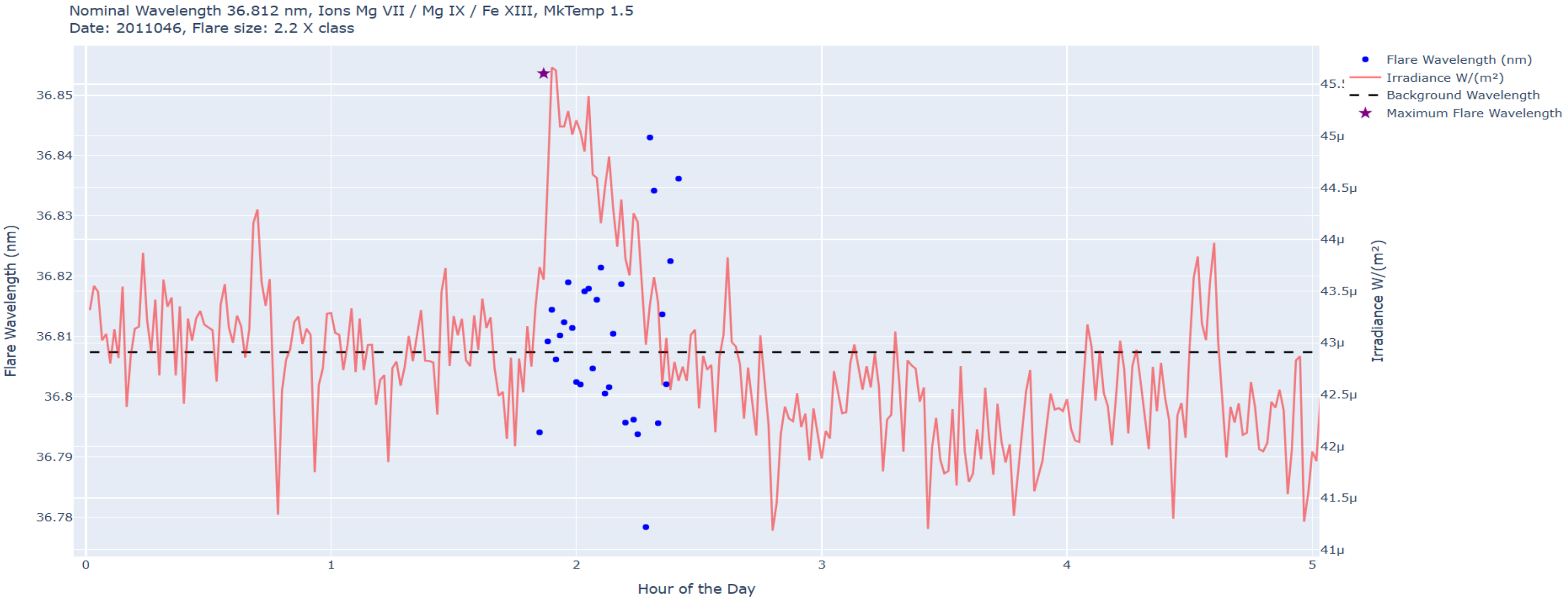

Figure 3.5: A flare wavelength (blue) and irradiance (red) graph for 36.812 nm on 2011/046. The maximum flare wavelength (purple star) and calculated background wavelength (black dashed line) are also included.

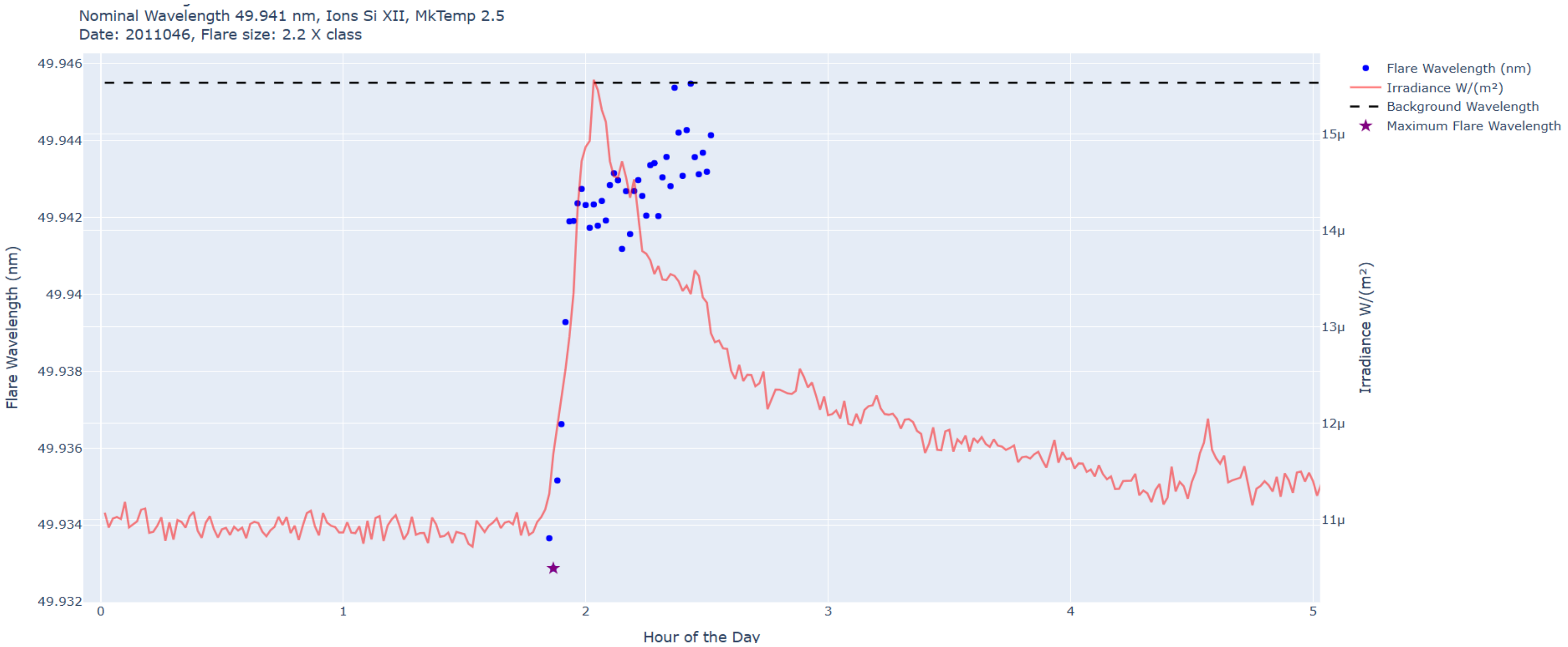

Figure 3.6: Like Figure 3.3, the Doppler behavior for 49.941 nm on 2011/046 is excessively clear. The inclusion of the background wavelength helps underscore the blueshift displayed.

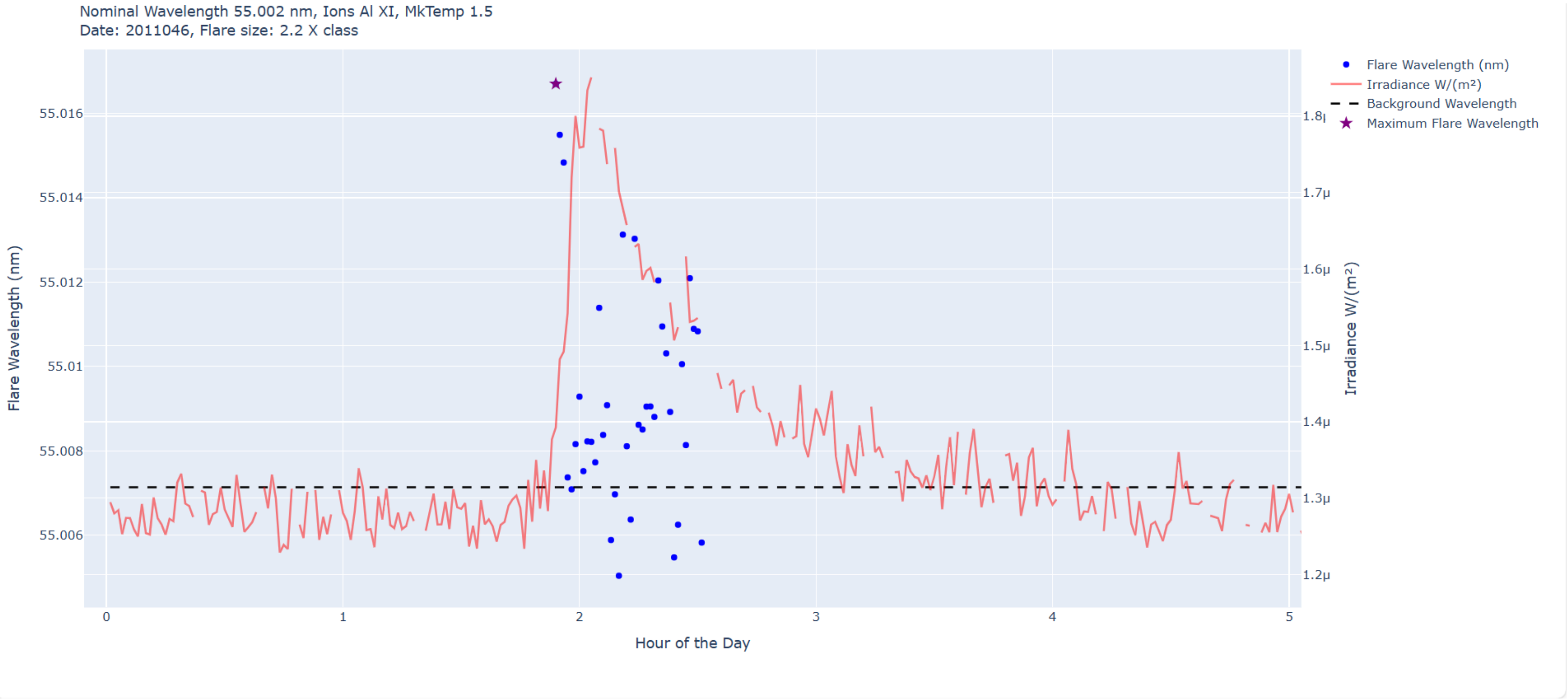

Figure 3.7: Flare wavelength and irradiance graph for 55.002 nm at 1.5 MK.

With the incorporation of the background wavelength instead of the nominal emission wavelength, the issue of uncertainty in the latter's value is eliminated. Additionally, the maximum flare wavelength value on the graphs provides a reference for the wavelength used by my code to determine the maximum Doppler Velocity for each date and ion (see Section 3.3). This value represents the maximum Doppler shift, whether red or blue, relative to the background wavelength.

Although the behavioral tendencies for the 1.5 MK temperature group on 2011/046 remain somewhat convoluted, overall analysis presents fewer challenges than when using the wavelength array. For 36.812 nm (Mg VII), Figure 3.5, the varying behavior from Figure 3.2 persists. The maximum flare wavelength occurs during a period of increasing flare irradiance and indicates a redshift. However, later values show both blue and redshifts. Some recorded values occur during the period of decreasing flare irradiance, or the gradual phase, which may imply ongoing heating of the chromosphere, affecting the nominal wavelength. Regarding 55.002 nm (Al XI), Figure 3.7, the behavior more closely follows the tentatively expected redshift. This line's maximum flare wavelength, along with many recorded values, shows an increase in wavelength from the background. As the irradiance returns to pre-flare conditions, blue-shifted values appear, though this is not inconsistent with current magnetic reconnection models. During the impulsive phase of this flare, the line corresponds to a downflow, resulting in a redshift. However, during the gradual phase, lines with formation temperatures between 0.3 and 4 MK can exhibit varying behavior, transitioning between downflows and upflows. This variability may be attributed to ongoing magnetic reconnection or other heating events, leading to the subsequent blueshift observed for Al XI. The 2 MK breakpoint distinguishing upflows from downflows in warm coronal lines is an estimate, and lower-temperature plasma near this threshold does not necessarily contradict existing models [17].

In contrast to the inconsistent Doppler shifts of 36.812 nm and 55.002 nm, the graph of 49.941 nm (Si XII) provides a clearer picture of the line's response to the flare (Figure 3.6). A clear decrease in wavelength is observed, corresponding to the predicted blueshift. The maximum flare wavelength is seen during the impulsive phase, and the measured wavelengths steadily increase as the flare enters the gradual phase.

While the flare wavelength and irradiance graphs are useful for interpreting the behavior of my nominal emission lines during a single flare, they offer limited insight into answering my overall research question. In contrast, Doppler Velocities serve as a much more valuable tool for this purpose.

3.3 Doppler Velocities:

The Doppler Velocities produced by the EVE data correlate to the relative flow speed of the plasma during the flare event; a full derivation for the flow speed with adjustments for spatial data can be found in [3]. Studying any relationships these velocities demonstrate when compared to flare magnitude remains of critical importance in advancing our understanding of solar physics. Concepts such as Hudson's Hot Prograde Shifts and the lack of a comprehensive model for magnetic reconnection stand to benefit from further characterization of solar plasma [3]. The detailed study of Doppler Velocities in relation to flare magnitude could help address these outstanding questions and contribute to the refinement of models that describe the behavior of the Sun's dynamic atmosphere.

$$V_{Doppler} = \frac{(\lambda_{Max} - \lambda_{Background}) * c}{\lambda_{Background}} \text{ (Eq.1)}$$

Note: λ_{Max} represents the maximum flare wavelength shift, $\lambda_{Background}$ is simply the background wavelength value calculated as mentioned in Section 3.2.

The maximum wavelength value is calculated by first subtracting the background wavelength from an array of flare wavelengths and then taking the absolute value of the resulting differences. From this new absolute value array, the index of the maximum value is identified and used to locate the corresponding wavelength in the unaltered flare wavelength array, determining the maximum shift—whether red or blue—relative to the background wavelength. By employing Eq.1, the Doppler Velocity for the nominal wavelength in question can be derived. A positive velocity equates to a redshift, as the maximum wavelength used is longer than the background, while a negative velocity gets associated with a blue shift due to the maximum wavelength being shorted than the calculated background.

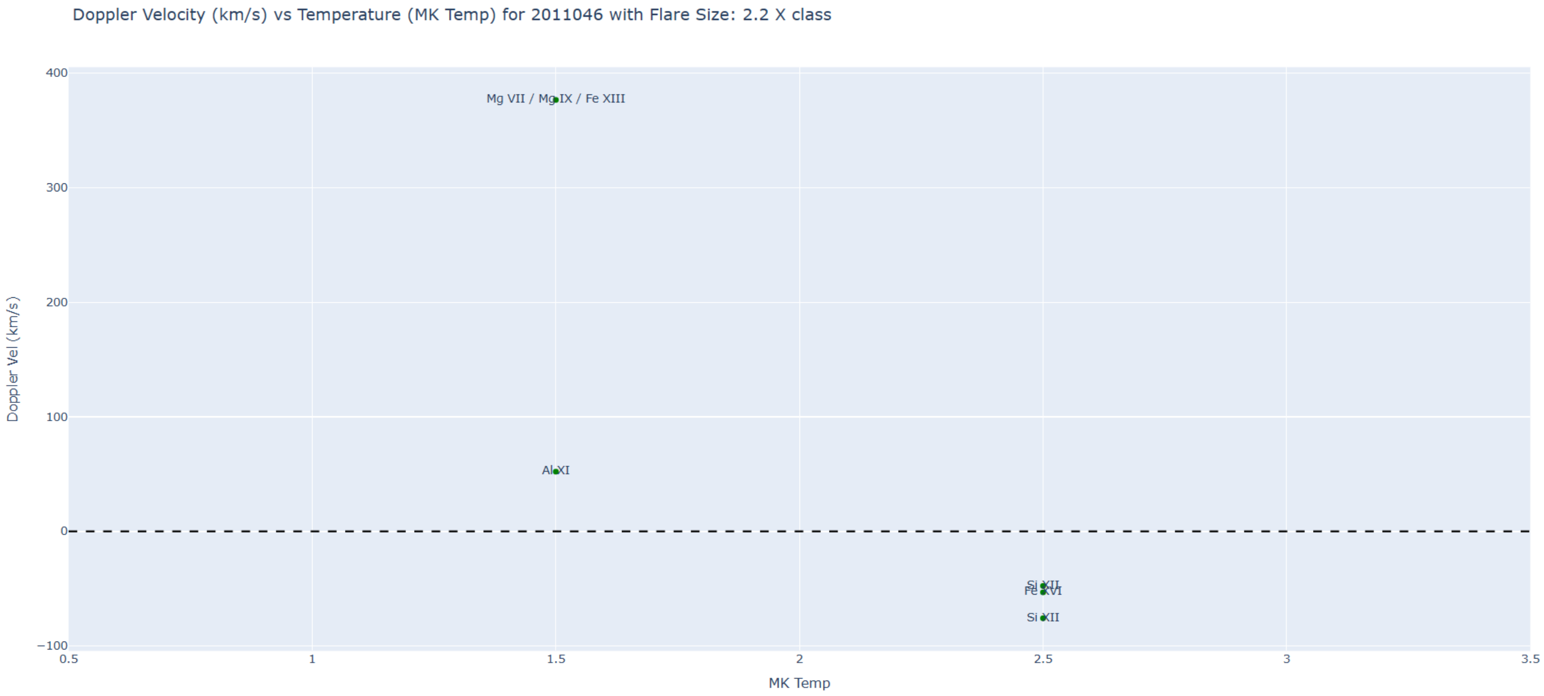

Figure 3.8: The derived Doppler Velocities are displayed for the five nominal wavelengths for a 2.2 X-class flare on 2011/046.

The Doppler Velocities observed in Figure 3.8 correspond to the maximum flare wavelength values discussed in the previous section. Similarly, the 1.5 MK group (Al XI and Mg VII) demonstrate a positive or redshifted Doppler Velocity, whereas the two Si XII lines and Fe VI line, observed at 2.5 MK, show a negative or blueshifted velocity.

To fully analyze any potential correlation between flare size and the magnitude of corresponding Doppler Velocities, I compiled a list of flare dates from the MEGS-B flare campaign website. This list covered a range of flare magnitudes and was aimed at distributing the dates evenly over the entirety of EVE's operational history (2010-2025). While this concept seemed straightforward in theory, it proved more challenging than anticipated. The EVE science team’s focus shifted following the loss of MEGS-A, as the 5-35 nm range was central to many of their studies. As a result, many of the earlier dates in the mission's history lacked complete spectra for MEGS-B. This posed a particular problem when attempting to set the background wavelength. Deriving this value depends on the ability to index the wavelength array with the pre-flare time, but when this pre-flare time fell during a period of MEGS-B inactivity, it rendered the calculation impossible.

Nevertheless, despite this obstacle, I meticulously worked through the data, finding valid dates that included measurements for all my selected nominal wavelengths, allowing me to continue with the analysis. Once I had gathered a sufficient collection of dates for C, M, and X class flares, I created a new Python function to graph Doppler Velocity vs. Flare Size. This process followed the same logic as before, though with modifications to produce a collective graph that covered all the selected dates.

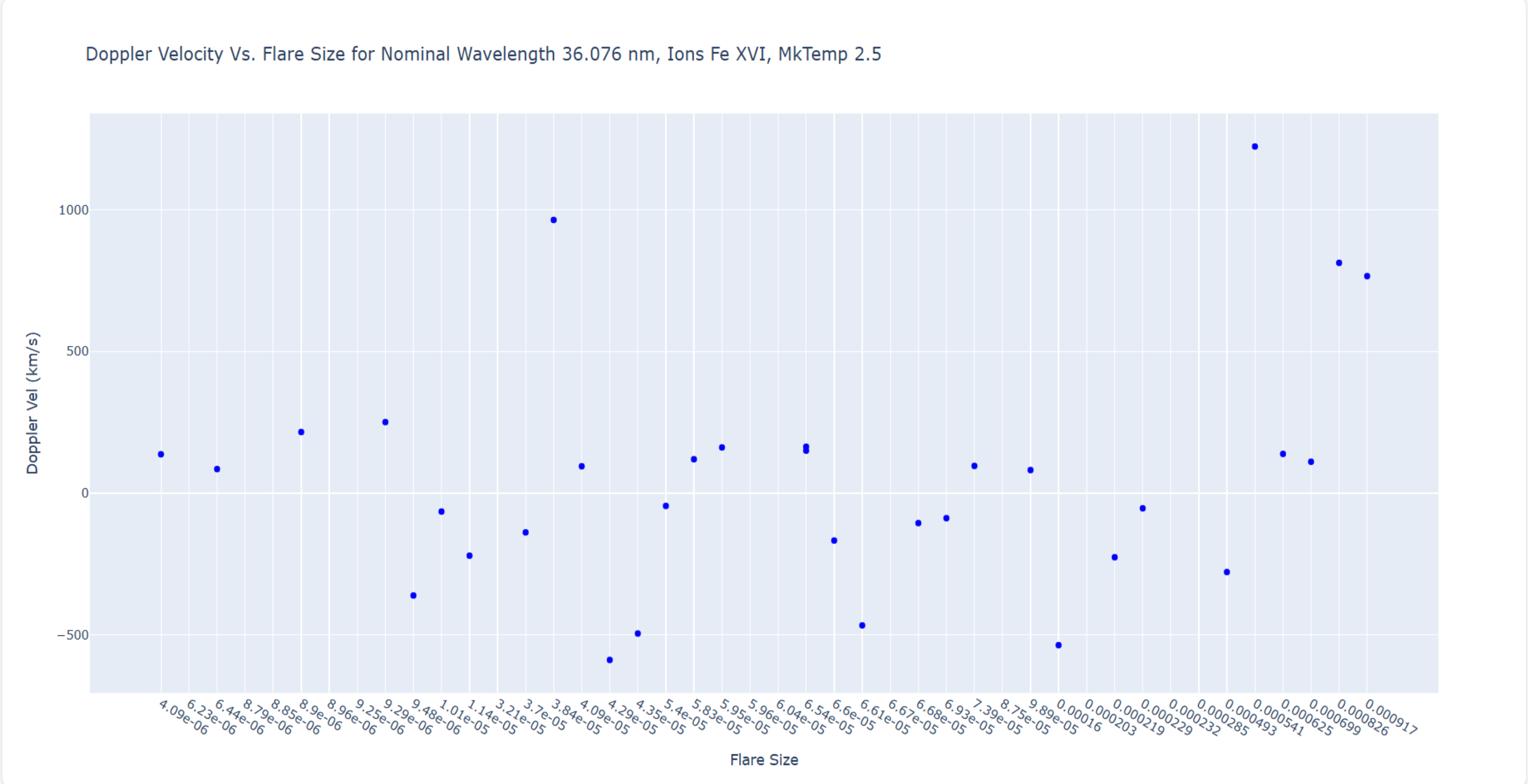

Figure 3.9: Doppler Velocity vs. Flare Size graph for 36.076 nm. No clear relationship is immediately discernible from this graph, as will be the trend for the following figures.

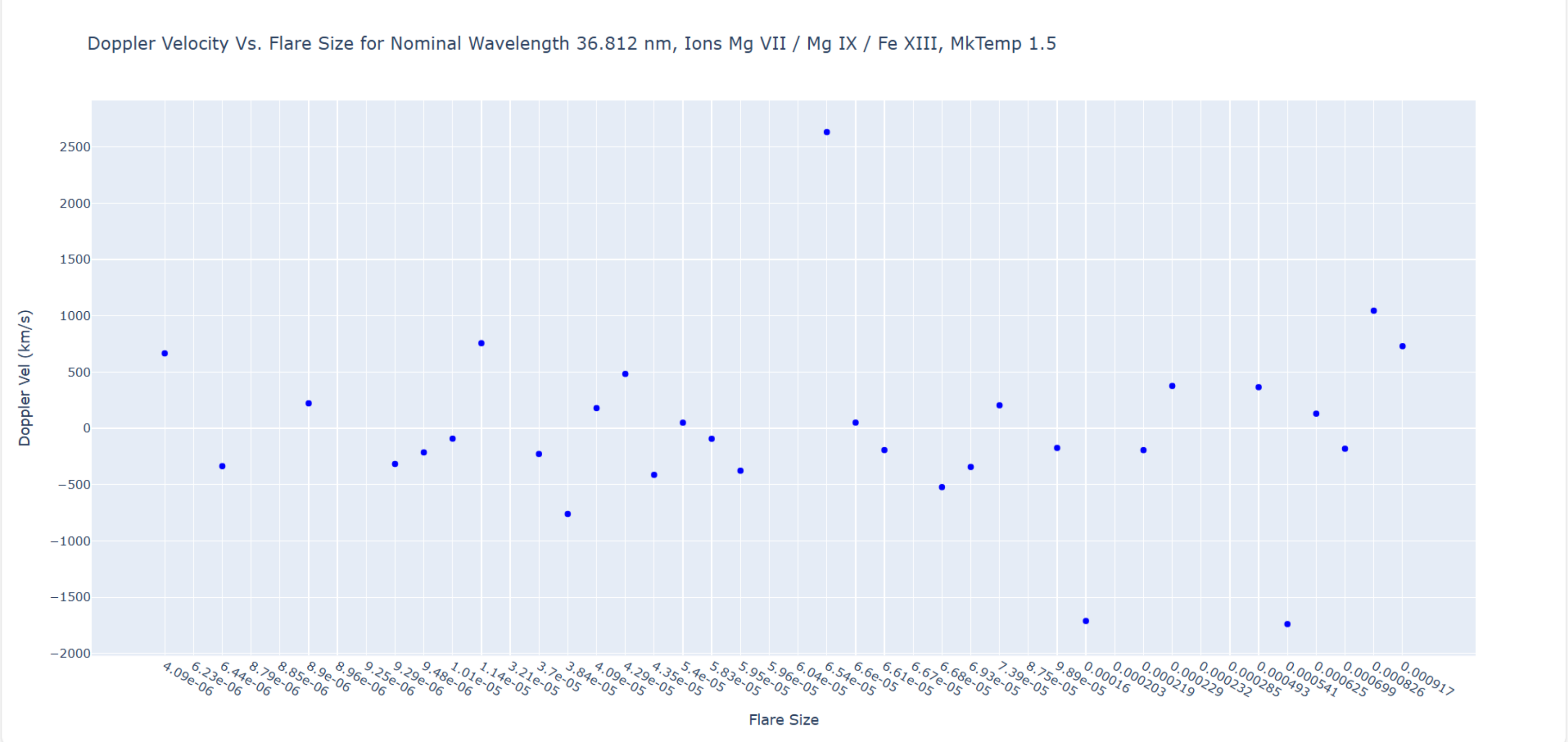

Figure 3.10: Doppler Velocity vs. Flare Size for 36.812 nm. It is important to note that the largest values represent both blue and redshifted velocities, as one might expect for the 1.5 MK group.

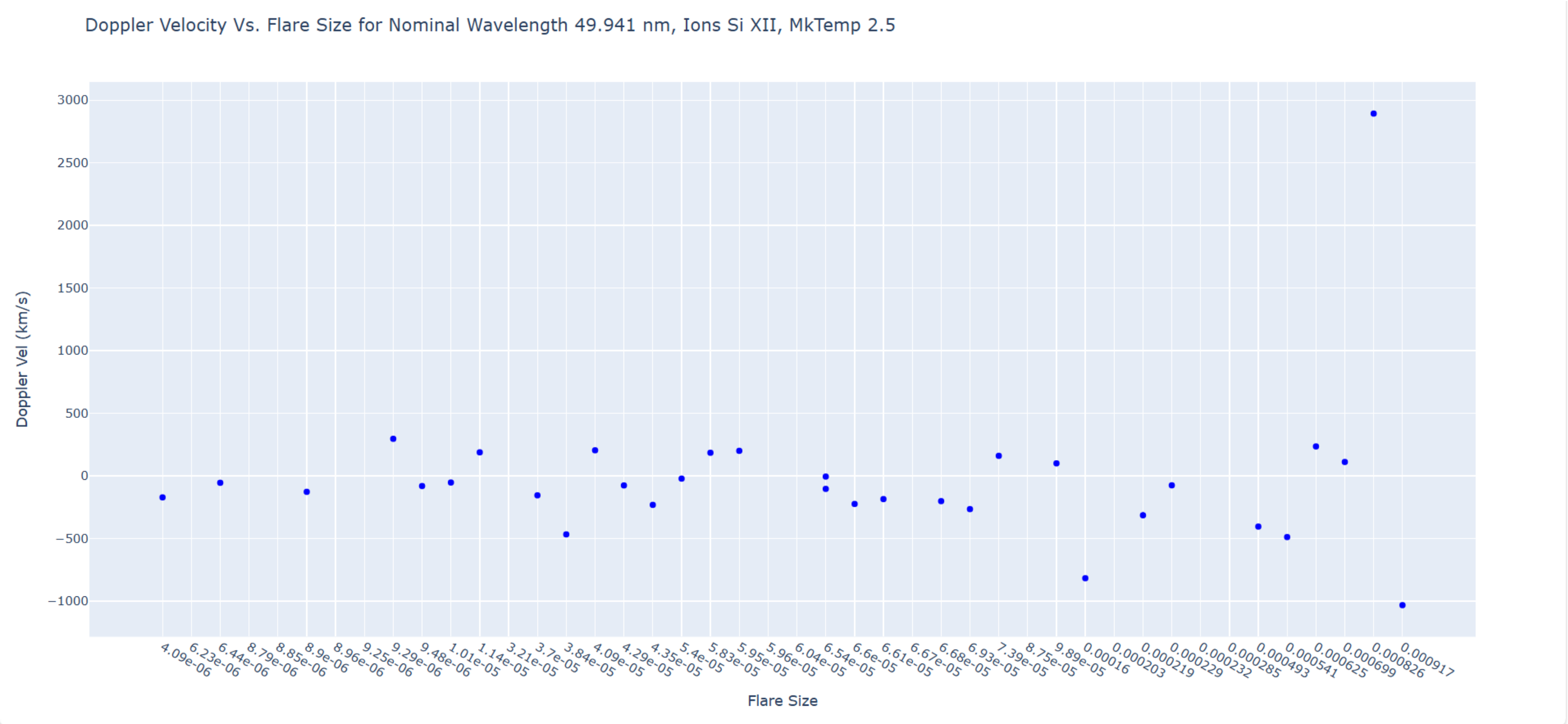

Figure 3.11: Doppler Velocity vs. Flare Size for 49.941 nm. Although apart of the 2.5 MK temperature group, the velocities appear almost evenly distributed between negative and positive values.

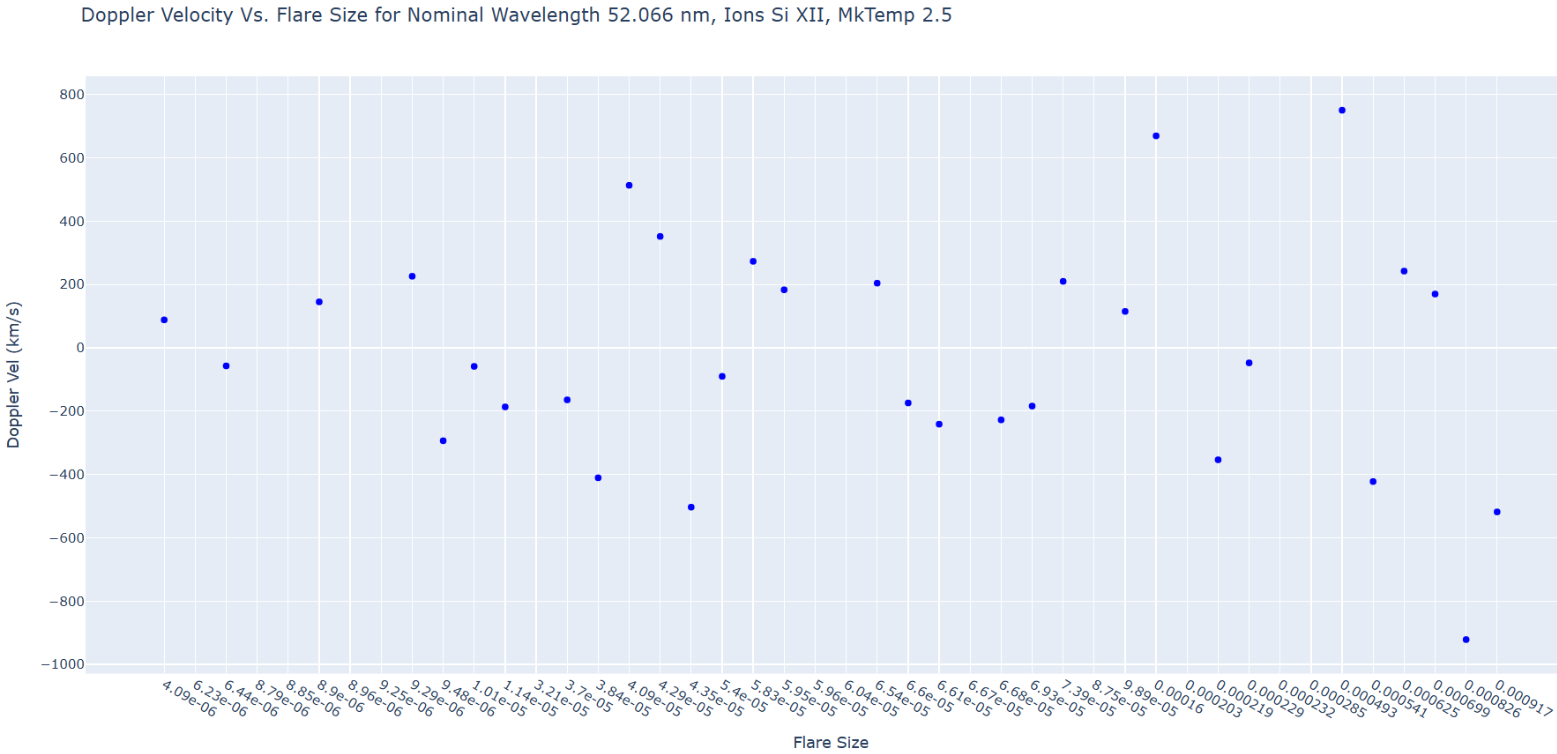

Figure 3.12: Doppler Velocity vs. Flare Size graph for 52.066 nm at 2.5 MK. At first glace the distribution looks entirely random, both in terms of magnitude and shift direction (blue or red).

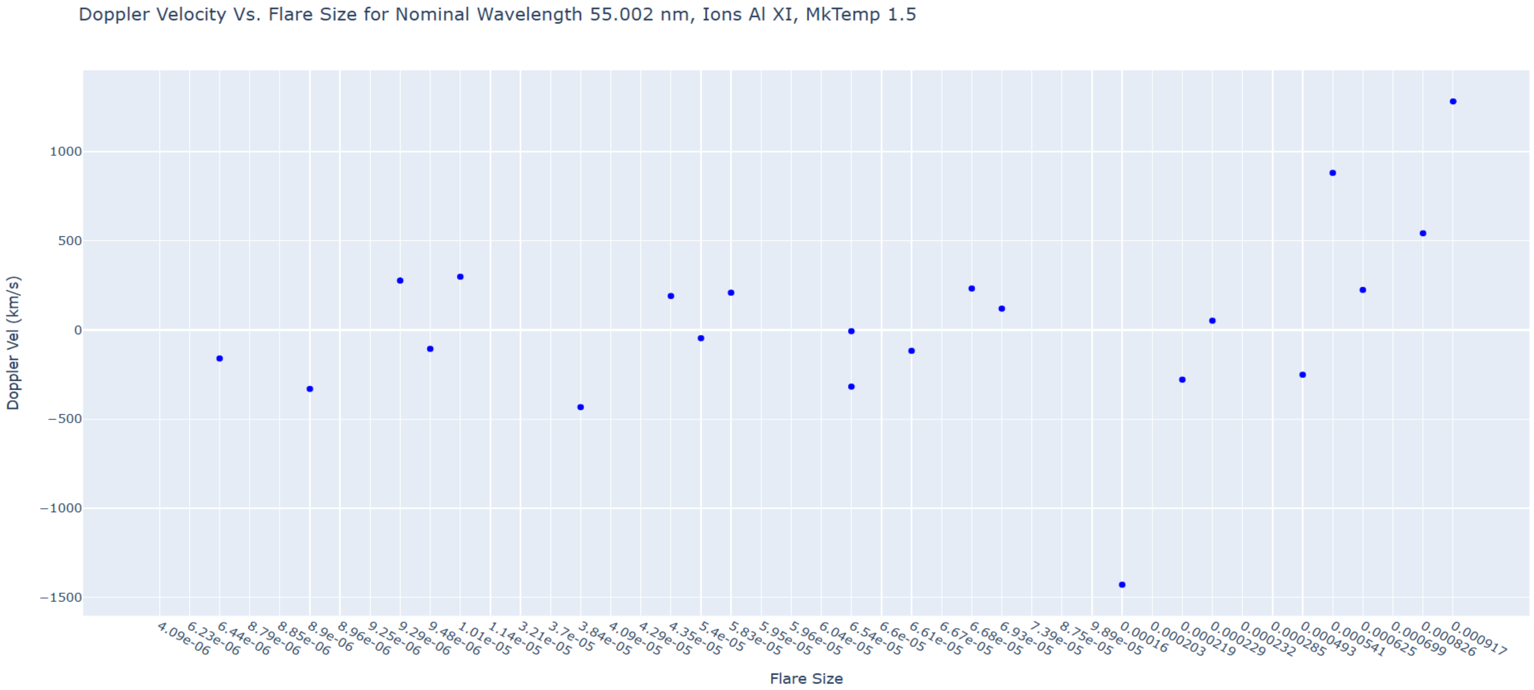

Figure 3.13: Doppler Velocity vs. Flare Size for 55.002 nm. Like Figure 3.11, the distribution between blue and redshifted velocities is not entirely unexpected. A seeming uptick in Doppler Velocity magnitude with the largest X-Cass flares in included is disproved in Figure 3.14.

To further facilitate the analysis of these figures, I also ran various correlation tests with the data. Specifically, I used both the Pearson and Spearman correlation coefficients. The logic behind this approach assumed that if a correlation did exist, it would either be linear (Pearson) or, at the very least, monotonic (Spearman). These tests helped provide a clearer understanding of the relationships between Doppler Velocities and flare magnitudes, and whether any significant statistical patterns could be identified from the data.

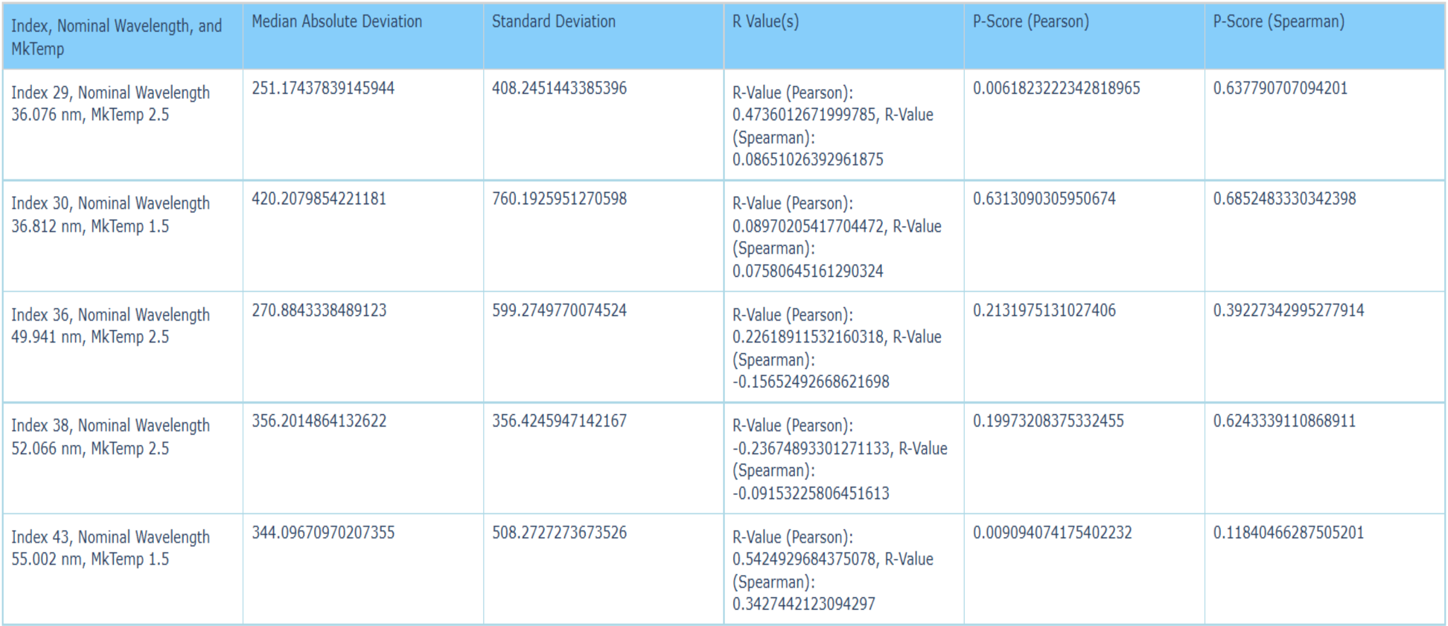

Index, Nominal Wavelength, and MkTemp	Median Absolute Deviation	Standard Deviation	R Value(s)	P-Score (Pearson)	P-Score (Spearman)
Index 29, Nominal Wavelength 36.076 nm, MkTemp 2.5	251.17437839145944	408.2451443385396	R-Value (Pearson): 0.4736012671999785, R-Value (Spearman): 0.08651026392961875	0.0061823222342818965	0.637790707094201
Index 30, Nominal Wavelength 36.812 nm, MkTemp 1.5	420.2079854221181	760.1925951270598	R-Value (Pearson): 0.08970205417704472, R-Value (Spearman): 0.07580645161290324	0.6313090305950674	0.6852483330342398
Index 36, Nominal Wavelength 49.941 nm, MkTemp 2.5	270.8843338489123	599.2749770074524	R-Value (Pearson): 0.22618911532160318, R-Value (Spearman): -0.15652492668621698	0.2131975131027406	0.39227342995277914
Index 38, Nominal Wavelength 52.066 nm, MkTemp 2.5	356.2014864132622	356.4245947142167	R-Value (Pearson): -0.23674893301271133, R-Value (Spearman): -0.09153225806451613	0.19973208375332455	0.6243339110868911
Index 43, Nominal Wavelength 55.002 nm, MkTemp 1.5	344.09670970207355	508.2727273673526	R-Value (Pearson): 0.5424929684375078, R-Value (Spearman): 0.3427442123094297	0.009094074175402232	0.11840466287505201

Figure 3.14: A table of correlation and statistical significance values. Each of my five nominal wavelengths has been evaluated, with its corresponding measurements displayed in the table.

From the figures, no clear relationship immediately presents itself between Doppler Velocity and flare size. This is further confirmed by the R correlation values seen in Figure 3.14. At first glance, the Pearson P-Score values seem to indicate that some form of statistical significance exists for nominal wavelengths 36.076 nm (Fe XVI) and 55.002 nm (Al XI), with P-Scores of 0.006 and 0.009, respectively. However, the other reference wavelengths for the same temperature group show no such relation. Similarly, the Spearman P-Score values indicate a lack of statistical significance between Doppler Velocity and flare magnitude.

Based on these findings, I conclude that no evident relationship exists between Doppler Velocity magnitude and solar flare size.

3.3.1: Error Propagation

To further substantiate my claims, I needed to analyze the error associated with the derived Doppler Velocities. The EVE product provides error values for both the flare wavelengths and wavelength arrays. To account for these errors, I propagated the error through the calculation of the maximum wavelength, as this involved subtracting the background wavelength from the measured flare wavelength (Eq. 2).

Once I had the propagated error for the maximum wavelength, I used this value in a subsequent propagation for the Doppler Velocity error (Eq. 3). This allowed for a more complete understanding of the uncertainty in the velocity measurements, ensuring that the conclusions drawn were not only based on the observed trends but also the accuracy of the data.

$$\sigma_{Max\ Wavelength\ Shift} = \sqrt{\sigma^2_{Flare\ Wavelength} + \sigma^2_{Background\ Wavelength}} \quad \text{(Eq. 2)}$$

$$\sigma_{Doppler} = V_{Doppler}\sqrt{\left(\frac{\sigma_{Max\ Wavelength\ Shift}}{\lambda_{Max\ Wavelength\ Shift}}\right)^2 + \left(\frac{\sigma_{Background\ Wavlength}}{\lambda_{Background\ Wavlength}}\right)^2} \quad \text{(Eq. 3)}$$

To incorporate the calculated error values into my correlation analysis, I used Python to create a Monte Carlo simulation with n = 1000. This method allowed me to randomly sample from the calculated error distributions and estimate the potential error values for both the R values and P-Scores.

By running the simulation, I generated a distribution of correlation values that accounted for the uncertainties in the Doppler Velocity and flare wavelength measurements. This approach helped assess the robustness of the observed correlations and provided a more comprehensive understanding of the potential variability in the data. Through this method, I was able to estimate the impact of error on the correlation results, giving a more accurate representation of the reliability of the derived R values and P-Scores.

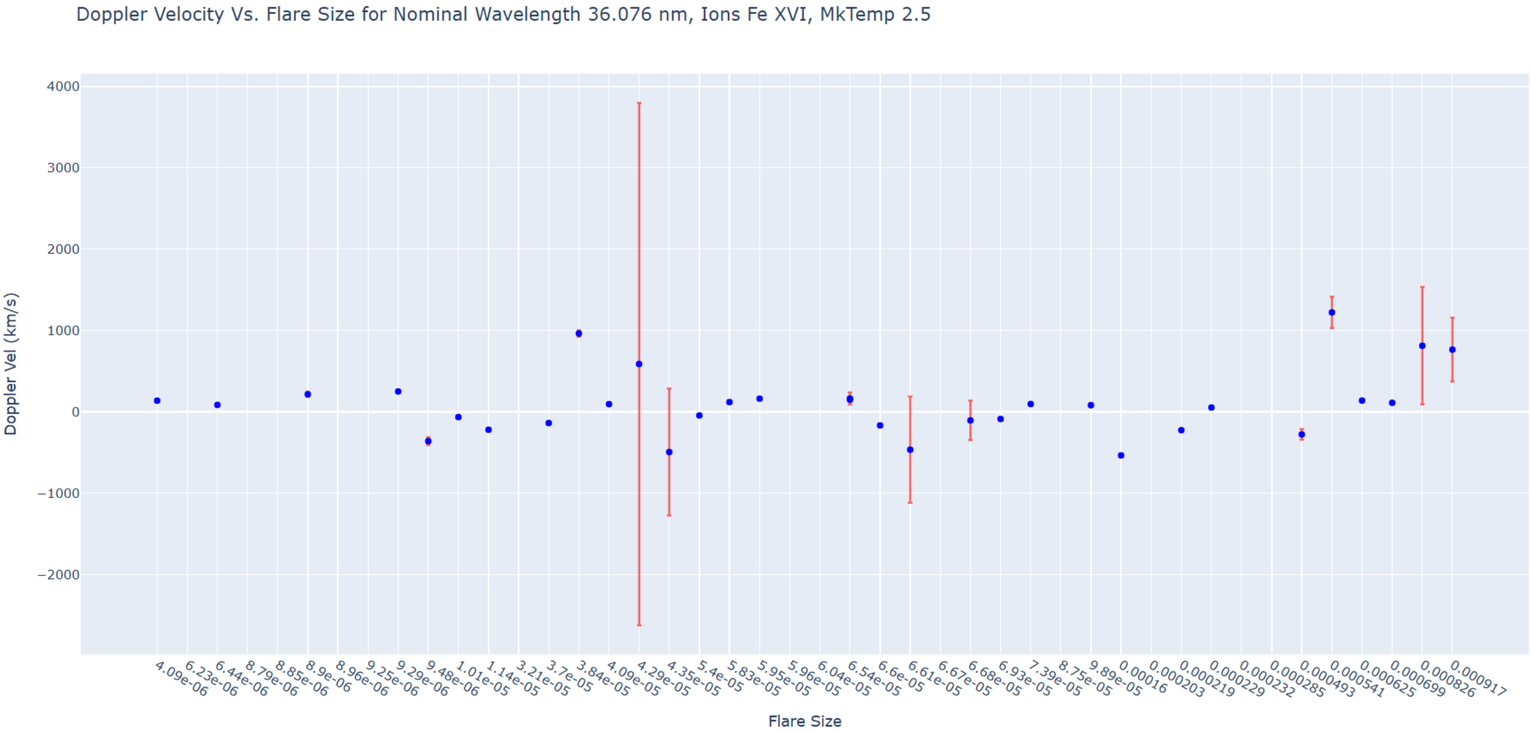

Figure 3.15: Doppler Velocity vs. Flare Size with error bars for 36.076 nm. Note that all points displayed do have error bars, however the incredibly large error of some values causes these to appear miniscule. For reference the largest error displayed is about +/-2000 km/s (100% of the measured value), and the average error is roughly 5-10% of the measured value.

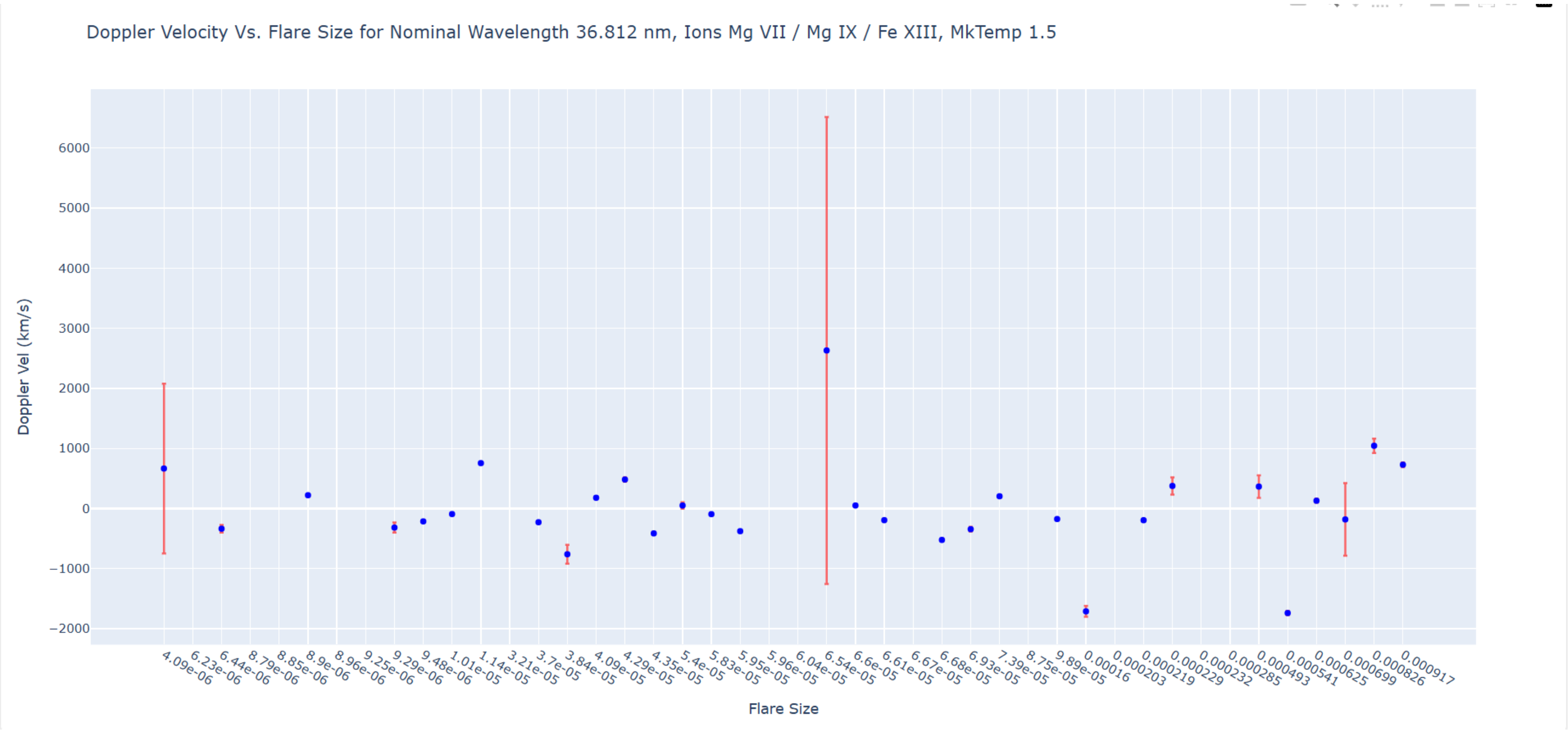

Figure 3.16: Doppler Velocity vs. Flare Size with error bars for 36.812 nm.

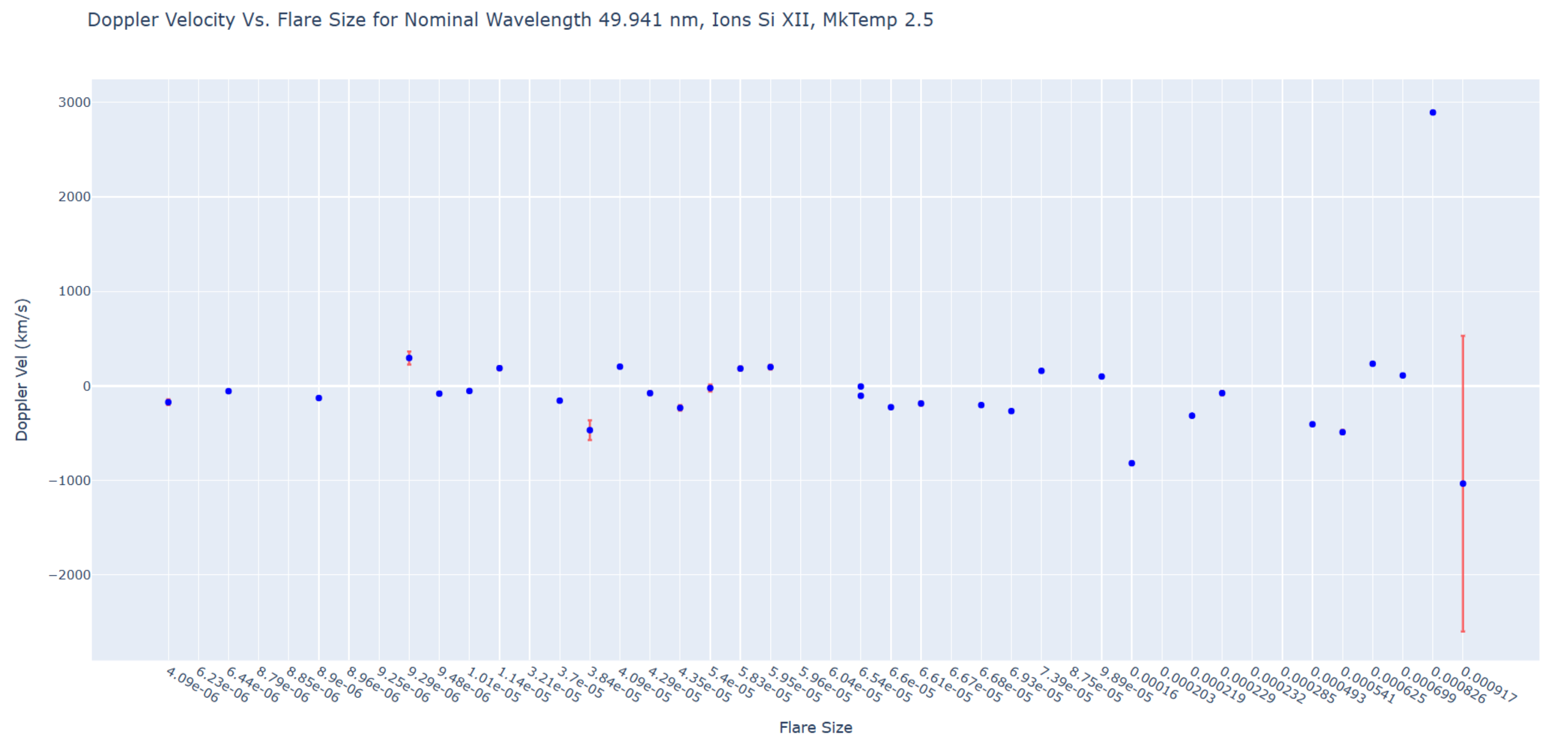

Figure 3.17: Doppler Velocity vs. Flare Size with error bars for 49.941 nm.

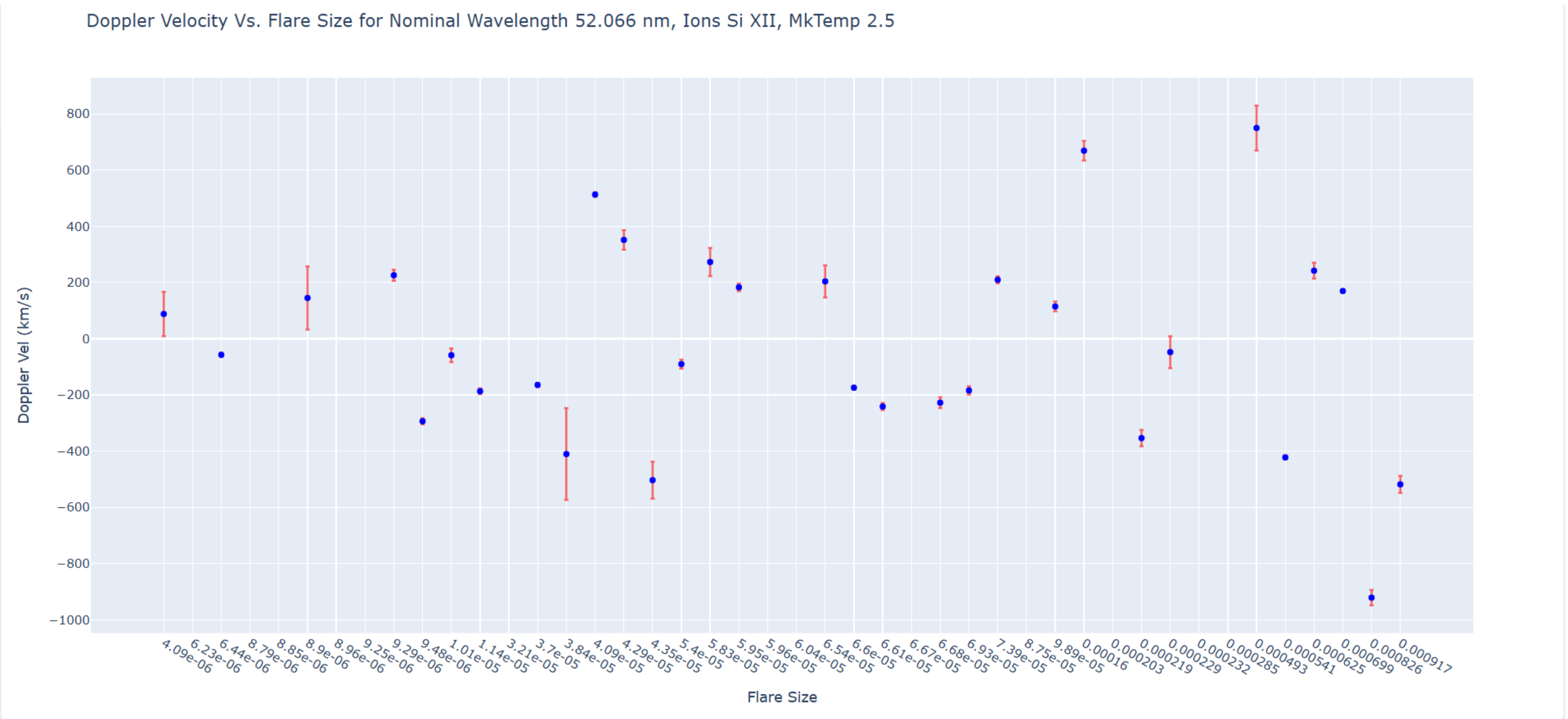

Figure 3.18: Doppler Velocity vs. Flare Size with error bars for 52.066 nm.

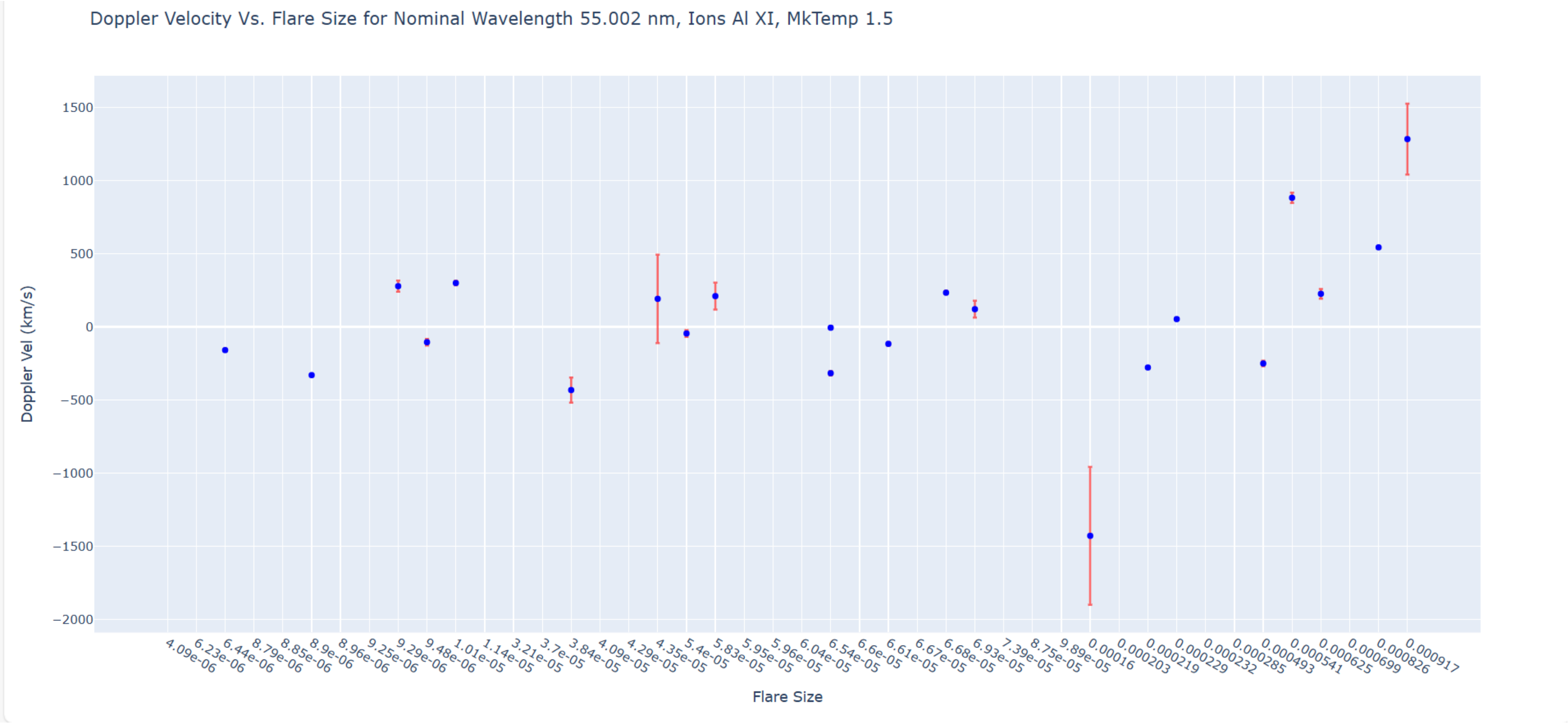

Figure 3.19: Doppler Velocity vs. Flare Size with error bars for 55.002 nm.

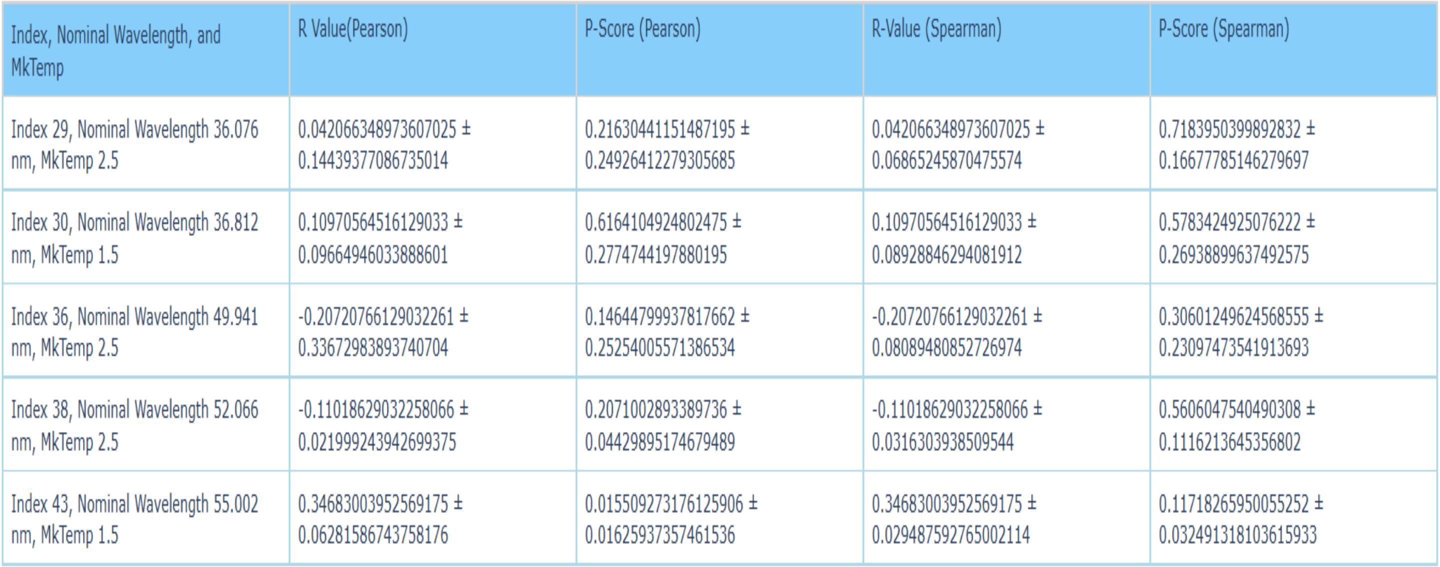

Index, Nominal Wavelength, and MkTemp	R Value(Pearson)	P-Score (Pearson)	R-Value (Spearman)	P-Score (Spearman)
Index 29, Nominal Wavelength 36.076 nm, MkTemp 2.5	0.042066348973607025 ± 0.14439377086735014	0.21630441151487195 ± 0.24926412279305685	0.042066348973607025 ± 0.06865245870475574	0.7183950399892832 ± 0.16677785146279697
Index 30, Nominal Wavelength 36.812 nm, MkTemp 1.5	0.10970564516129033 ± 0.09664946033888601	0.6164104924802475 ± 0.2774744197880195	0.10970564516129033 ± 0.08928846294081912	0.5783424925076222 ± 0.26938899637492575
Index 36, Nominal Wavelength 49.941 nm, MkTemp 2.5	-0.20720766129032261 ± 0.33672983893740704	0.14644799937817662 ± 0.25254005571386534	-0.20720766129032261 ± 0.08089480852726974	0.30601249624568555 ± 0.23097473541913693
Index 38, Nominal Wavelength 52.066 nm, MkTemp 2.5	-0.11018629032258066 ± 0.021999243942699375	0.2071002893389736 ± 0.04429895174679489	-0.11018629032258066 ± 0.0316303938509544	0.5606047540490308 ± 0.1116213645356802
Index 43, Nominal Wavelength 55.002 nm, MkTemp 1.5	0.34683003952569175 ± 0.06281586743758176	0.015509273176125906 ± 0.01625937357461536	0.34683003952569175 ± 0.029487592765002114	0.11718265950055252 ± 0.032491318103615933

Figure 3.20: A table of correlation and statistical significance values with error values found through Monty Carlo simulation. Each of my five nominal wavelengths has been evaluated, with its corresponding measurements displayed in the table.

The Doppler Velocity error values in my analysis averaged around 1-5% of the measured value, with some noticeable outliers in the data. This indicates that while the error margin is relatively small, there are occasional significant deviations. However, these error values do not drastically alter the overall interpretation, suggesting that the calculated correlation values without error are reasonably accurate approximations of the actual relationships between Doppler Velocity and flare size.

Critically, when accounting for the error values, the statistical significance previously indicated for 36.076 nm (Fe XVI) no longer holds, as the Pearson P-Score no longer suggests a significant correlation. On the other hand, the 55.002 nm (Al XI) line still maintains a P-Score of 0.015, which is desirable (below the typical 0.05 threshold for significance), even after accounting for the error. However, when cross comparing this value with the other 1.5 MK line (36.812 nm), the significance becomes questionable.

In conclusion, my analysis confirms that, even with the Monte Carlo simulation and error propagation, there is no clear relationship between flare size and Doppler Velocity. The correlation values and P-Scores, when adjusted for error, show that the initial observed trends were not robust enough to support a significant link between these variables. Therefore, I reject the hypothesis of a direct correlation between Doppler Velocity and flare size.

4: Conclusions

4.1: Relationship Between Flare Size and Magnitude of Corresponding Doppler Velocities

As noted in the previous sections, the analysis of the correlation and statistical significance values for Doppler Velocity and flare size produced little evidence to support a relationship between the two. This conclusion applies to both the 1.5 MK and 2.5 MK groups evaluated in this paper. However, I present these results as preliminary due to several key limitations in the study.

First, the sample size of both flares and nominal wavelengths considered in this analysis was limited, which may have reduced the power of the statistical tests. Additionally, despite efforts to minimize their influence, line blends in the data could still be affecting the results. The 0.1 nm spectral resolution of the EVE instrument, combined with the complex nature of solar flare emissions, makes it challenging to fully eliminate blends or to account for their subtle effects on Doppler shifts.

Given these constraints, I believe more data—with a higher spectral resolution and a larger variety of flares—would be required to provide a more conclusive answer. Future studies incorporating these factors could help confirm or refine the results of this analysis, offering a more robust understanding of any potential relationship between Doppler Velocity and flare magnitude.

4.2: Future Research

In my figures of Doppler Velocity vs. Flare Size, one might note that a consistent, blue-shifted velocity cannot be found in the 2.5 MK group (Figures 3.9, 3.11, and 3.12). Although the 1.5 MK group does not exhibit the expected redshifted velocity, research on lines with temperatures above the roughly estimated 2.0 MK cutoff has been more extensive, and their blueshifted Doppler behavior is better established. I believe that a possible refinement of the data product, along with improvements to my code (such as eliminating poorly fit flare wavelengths), could help clarify these discrepancies. Additionally, limiting the maximum flare wavelength to those during the impulsive phase could provide better insight into the lack of expected, blue-shifted behavior in the 2.5 MK group.

Furthermore, extending the scope of my research to include Coronal Mass Ejections (CMEs) could present an interesting avenue for future investigation. Catalogs of CME events already exist, and by combining this data with spatial information from the AIA (Atmospheric Imaging Assembly), it would be possible to correlate nominal wavelength measurements with specific CMEs. While my findings do not currently suggest a relationship between CMEs and the magnitude of corresponding Doppler Velocities, exploring this potential link would undoubtedly offer new insights into solar physics and the dynamics of the solar atmosphere.

5: Bibliography

[1] P. A. Cassak, Y.-H. Liu, and M. A. Shay, A review of the 0.1 reconnection rate problem, J. Plasma Phys. **83**, 715830501 (2017).

[2] F. Fang, W. Manchester, W. P. Abbett, and B. Van Der Holst, BUILDUP OF MAGNETIC SHEAR AND FREE ENERGY DURING FLUX EMERGENCE AND CANCELLATION, ApJ **754**, 15 (2012).

[3] H. S. Hudson, S. M. Mulay, L. Fletcher, J. Docherty, J. Fitzpatrick, E. Pike, M. Strong, P. C. Chamberlin, and T. N. Woods, Fast prograde coronal flows in solar active regions, Monthly Notices of the Royal Astronomical Society: Letters **515**, L84 (2022).

[4] M. Yamada, R. Kulsrud, and H. Ji, Magnetic reconnection, Rev. Mod. Phys. **82**, 603 (2010).

[5] E. Priest, *Magnetohydrodynamics of the Sun*, 1st ed. (Cambridge University Press, 2014).

[6] B. Chen et al., Measurement of magnetic field and relativistic electrons along a solar flare current sheet, Nat Astron **4**, 1140 (2020).

[7] T. G. Forbes, The nature of Petschek-type reconnection, Earth Planet Sp **53**, 423 (2014).

[8] E. P. Kontar, J. E. Perez, L. K. Harra, A. A. Kuznetsov, A. G. Emslie, N. L. S. Jeffrey, N. H. Bian, and B. R. Dennis, Turbulent Kinetic Energy in the Energy Balance of a Solar Flare, Phys. Rev. Lett. **118**, 155101 (2017).

[9] *Plasma Simulation Lab.—Research—Magnetic Reconnection*, https://rnumata.org/research/recon.

[10] S. Molokov, R. Moreau, and H. K. Moffatt, *Magnetohydrodynamics: Historical Evolution and Trends* (Springer, Dordrecht, 2007).

[11] P. H. Roberts, *Alfvén's Theorem and the Frozen Flux Approximation*, in *Encyclopedia of Geomagnetism and Paleomagnetism*, edited by D. Gubbins and E. Herrero-Bervera (Springer Netherlands, Dordrecht, 2007), pp. 7–11.

[12] T. Alboussière, *Course 1 Fundamentals of MHD*, in *Les Houches*, Vol. 88 (Elsevier, 2008), pp. 1–44.

[13] R. M. Kulsrud, Magnetic reconnection: Sweet-Parker versus Petschek, Earth Planet Sp **53**, 417 (2014).

[14] H. S. Hudson, T. N. Woods, P. C. Chamberlin, L. Fletcher, G. Del Zanna, L. Didkovsky, N. Labrosse, and D. Graham, The EVE Doppler Sensitivity and Flare Observations, Sol Phys **273**, 69 (2011).

[15] T. N. Woods et al., Extreme Ultraviolet Variability Experiment (EVE) on the Solar Dynamics Observatory (SDO): Overview of Science Objectives, Instrument Design, Data Products, and Model Developments, Sol Phys **275**, 115 (2012).

[16] P. C. Chamberlin et al., Solar Ultraviolet Irradiance Observations of the Solar Flares During the Intense September 2017 Storm Period, Space Weather **16**, 1470 (2018).

[17] L. Fletcher, Solar Flare Spectroscopy, Annual Review of Astronomy and Astrophysics **62**, 437 (2024).